Joint multifractal measures: Theory and applications to turbulence

Charles Meneveau,* K. R. Sreenivasan, P. Kailasnath, and M. S. Fan
Mason Laboratory, Yale University, New Haven, Connecticut 06520
(Received 5 July 1989)

A high-Reynolds-number turbulent flow subsumes several intermittent fields; some examples are the rates of dissipation of turbulent energy and scalar variance, square of turbulent vorticity and rate of strain, etc. These intermittent fields display different degrees of correlation among them. Motivated by the need for characterizing such coexisting distributions of intermittent fields in fully developed turbulence, the multifractal formalism—which we have already found useful in describing such intermittent distributions singly—is extended to more than one variable. The formalism is first illustrated by studying joint log-normal as well as joint binomial distributions. It is then applied to simultaneous measurements in several classical turbulent flows of the joint distribution of a component of the dissipation of kinetic energy, the dissipation rate of passive scalar variance, as well as the square of a component of turbulent vorticity. This allows simple but realistic models of simultaneous cascades of more than one variable to be developed.

I. INTRODUCTION

Multifractal measures arise in a variety of applications. Distributions whose moments scale in a nontrivial fashion were used by Mandelbrot[1] to characterize the spatial distribution of dissipation in turbulence. A geometric interpretation of such distributions in terms of interwoven sets of singularities with varying dimensions was then proposed by Frisch and Parisi,[2] who coined the name *multifractals*. These ideas were then used to describe the scaling of velocity-structure functions in turbulent flows.[3] In dynamical systems, such concepts were shown to be useful in characterizing the invariant measure of chaotic attractors.[3,4] This has also been applied to experiments on the transition to chaos in closed and open fluid flows.[5,6] In fractal growth processes like diffusion-limited aggregation the probability distribution of growth has been shown[7] to be multifractal in many instances. For a general account of the wide range of applications of multifractals, the reader is referred to the review article by Paladin and Vulpiani.[8]

The multifractal nature of the dissipation rate ε of kinetic energy in fully developed turbulence was studied experimentally in Ref. 9 using linear sections through a variety of turbulent flows. The relevance of these findings to the singularities of the equations of fluid motion was discussed in Ref. 10, and it was shown that one can model the multifractal spectrum obtained from linear cuts in terms of binomial cascades.[11] For an extension to multinomial models, see Ref. 12. Using both planar and linear sections, the dissipation rate χ of passive scalar fluctuations was also shown to be multifractal.[13,14] Further, there is experimental evidence that the field of squared vorticity (or its absolute value) can also be described by multifractal measures.[15] Thus, in turbulent flows, there appears to be a variety of multifractal measures embedded in the same spatial domain. As an example, we show in Figs. 1(a) and 1(b) typical segments of (a single term each of) ε and χ along the *same* linear cut in a fully developed turbulent flow. (For convenience, experimental details are relegated to a subsequent section.) The question then naturally arises about the degree of correlation among these different quantities. In other words, we are interested in the joint statistics of two or more such quantities, each of which is singly represented by a multifractal.

The natural way of describing such situations is to extend the multifractal formalism to more than one variable, this being the main purpose of the paper. The basic theory of joint multifractal measures is presented in Sec. III, and illustrated with simple special cases in Sec. IV. Section V deals with application of these ideas to measurements in a heated turbulent wake, where the joint

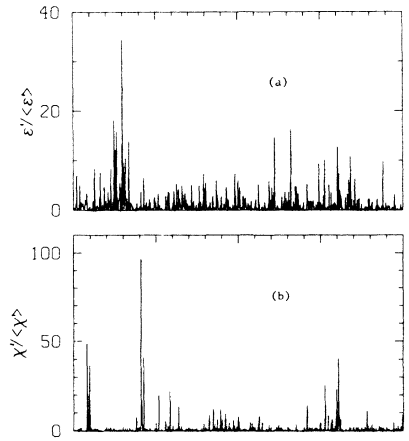

FIG. 1. Simultaneous signals of $\varepsilon' \sim (\partial u_1/\partial t)^2$ and $\chi' \sim (\partial T/\partial t)^2$ obtained in the turbulent wake of a heated cylinder, both normalized by their mean values. The segment of data shown corresponds to a length of approximately $10L$, where L is the integral scale of the flow estimated from the autocorrelation of the velocity signal.

multifractal distribution of the dissipation of kinetic energy, as well as the dissipation of passive scalar fluctuations, is presented. Section VI deals with the joint multifractal distribution of the dissipation and squared vorticity in measurements performed in the atmospheric surface layer. These measurements have been performed only on single components of the dissipation and vorticity. The conclusions are contained in Sec. VII. But first, a brief review of the multifractal formalism for single multifractal distribution is presented in Sec. II, where we also provide a useful definition of intermittency exponents in terms of the statistics of the local singularity strengths.

II. BRIEF REVIEW OF SINGLE MULTIFRACTAL MEASURES

Multifractal distributions are best described by the scaling properties of coarse-grained measures. Typically, if $p_r(x_i)$ is the measure in a box of size r centered around position x_i, one can define α as a local singularity strength at position x_i by[4]

$$p_r(x) \sim (r/L)^{\alpha} . \tag{1}$$

Here L is some large scale. Typically,[4] the set of boxes where α has values within a band $d\alpha$ around α has a fractal dimension $f(\alpha)$. This means that the number $N_r(\alpha)d\alpha$ of boxes of size r that contain values of α in that range scale according to

$$N_r(\alpha)d\alpha \sim (r/L)^{-f(\alpha)}d\alpha . \tag{2}$$

The total number of boxes of size r in the entire space of dimension d is proportional to $(r/L)^{-d}$. Therefore, the probability $\Pi_r(\alpha)d\alpha$ of encountering values α in such a band $d\alpha$ in some box scales as

$$\Pi_r(\alpha)d\alpha \sim (r/L)^{d-f(\alpha)}d\alpha . \tag{3}$$

Several cautionary notes must be made when interpreting the exponent $f(\alpha)$ as a fractal dimension: The first is that $f(\alpha)$ relates to the scaling behavior of $N_r(\alpha)$ or $\Pi_r(\alpha)$ only when α is defined according to (1) using the same resolution r used to compute $N_r(\alpha)$ or $\Pi_r(\alpha)$. This means that $f(\alpha)$ cannot be measured by defining an iso-α set using Eq. (1) at some resolution $r=\eta$, say, and then covering this fixed set with boxes of varying sizes $r'>\eta$, counting them to obtain $N_{r'(\alpha)}$, and then obtaining $f(\alpha)$ from $N_{r'}(\alpha) \sim (r')^{-f(\alpha)}$. In such a case one measures another effective exponent (for a detailed analysis of this issue, see Ref. 16). The second note is that there exist distributions for which $f(\alpha)$ can take negative values; for such cases $f(\alpha)$ cannot be interpreted as a dimension, but $d-f(\alpha)$ is still the scaling exponent of $\Pi_r(\alpha)$.[17] Finally, it has been shown[18] that the scaling relations (2) and (3) have logarithmic prefactors that depend on $\ln(r/L)$, which complicate the direct measurement of $f(\alpha)$ from such relations. We will return to this issue below.

On the other hand, the scaling of the qth "cumulant" of $p_r(x_i)$ with the box size r involves the exponents $\tau(q)$ according to[19]

$$\sum_i [p_r(x_i)]^q \sim (r/L)^{\tau(q)} , \tag{4}$$

$$\langle p_r(x_i)^q \rangle \sim (r/L)^{\tau(q)+d} , \tag{5}$$

where the sum and averaging are performed over all boxes. Also, it is often convenient to define a set of exponents D_q according to

$$D_q = \tau(q)/(q-1) . \tag{6}$$

The exponents D_q are usually called "generalized dimensions," and correspond to the dimension of a set which, when used to intersect the original measure, produces divergence of moments of order q (see Ref. 17). In addition, if the support of the measure is a fractal set with fractal dimension $D_{q=0}<d$, then the total number of nonempty boxes [where $p_r(x)\neq 0$] is proportional to $(r/L)^{-D_0}$. In such cases, one replaces d in Eqs. (3) and (5) by D_0.

One can relate the exponents $\tau(q)$, α, and $f(\alpha)$ by evaluating averages as integrals over all values of α, and using the method of steepest descent for small values of r. One then obtains[4]

$$f(\alpha(q)) = q\alpha(q) - \tau(q) , \tag{7a}$$

and

$$\alpha(q) = \frac{d\tau(q)}{dq} . \tag{7b}$$

These relations form a Legendre transformation. [One replaces a function $\tau(q)$ by its slope α and its intercept $f(\alpha)$.] The parameter q selects a specific value of the variable α according to Eq. 7(b). High positive values of q emphasize high-intensity regions of the measure (low values of α), and high negative values of q emphasize low-intensity regions of the measure (high values of α).

According to Eq. (4), $\tau(q)$ can be measured from log-log of $\sum_i [p_r(x_i)]^q$ vs r/L. Then α and $f(\alpha)$ are usually computed using Eqs. (7). In principle, one can obtain α and $f(\alpha)$ directly from the scaling relations (1) and (2), but in Ref. 18 this was shown to be practical only when the available scaling range is very large, this being so because of the logarithmic prefactors in Eq. (2). Another method of directly measuring α and $f(\alpha)$ using μ-weighted averaging was proposed in Ref. 20 and applied to turbulence in Ref. 21. In this method, one defines a new normalized variable $\mu_r(x_i;q)$ in terms of the original multifractal measure according to

$$\mu_r(x_i;q) = \frac{p_r(x_i)^q}{\sum_i p_r(x_i)^q} . \tag{8}$$

Again, $\mu_r(x_i;q)$ varies from box to box, but it also depends on the parameter q. One now computes α as the mean value of $\ln[p_r(x_i)]/\ln(r/L)$ with respect to this measure $\mu_r(x_i;q)$. This is given by

$$\alpha(q) = \sum_i [\mu_r(x_i;q)\ln(p_r)/\ln(r/L)] , \tag{9}$$

where the sum is performed over all boxes of size r. Recalling that

$$\tau(q)=\ln(\sum_i p_r^q)/\ln(r/L)$$

(in the limit of $r\to 0$) and taking its derivative with respect to q, it is easy to show that the definition (9) coincides with $\alpha(q)$ obtained earlier from Eq. (7b). In order to compute the dimensionality associated with this value of $\alpha(q)$ one uses the usual definition of the dimension of a measure

$$\dim[\mu_r(x;q)]=\lim_{r\to 0}\frac{\sum_i[\mu_r(x_i;q)\ln\mu_r(x_i;q)]}{\ln(r/L)}\ , \qquad (10)$$

where, again, the sum is taken again over all boxes of size r. It is now easy to show, using the definition of the moment exponents $\tau(q)$ and the Legendre transform, that $\dim[\mu_r(x;q)]$ is equal to the exponent $f(\alpha)$ computed according to Eq. (7a). Thus, in practice, α and $f(\alpha)$ can be directly measured as slopes of plots of numerators of Eqs. (9) and (10) against $\ln(r/L)$. Such a procedure does not suffer from the influence of prefactors.

Another interesting question concerns moments of the local scaling exponent α itself. For this purpose, it is useful to introduce the following generating function[12] $G(q)$:

$$G(q)=\int_\alpha \rho(\alpha)(r/L)^{q\alpha-f(\alpha)+D_0}d\alpha\ , \qquad (11)$$

where, as noted before, D_0 is the fractal dimension of the support of the measure. We first consider derivatives of $G(q)$ with respect to q, evaluated at $q=0$:

$$\left.\frac{dG(q)}{dq}\right|_{q=0}=\ln(r/L)\int_\alpha \alpha\rho(\alpha)(r/L)^{-f(\alpha)+D_0}d\alpha\ . \qquad (12)$$

It is easily recognized that the integral corresponds to $\langle\alpha\rangle$, averaged over all nonempty boxes of the measure. From the evaluation of the integral in Eq. (11) using the steepest-descent method, we also know that

$$G(q)=(r/L)^{\tau(q)+D_0}\ , \qquad (13)$$

and that

$$\left.\frac{dG(q)}{dq}\right|_{q=0}=\ln(r/L)\left.\frac{d\tau(q)}{dq}\right|_{q=0}\ . \qquad (14)$$

Comparing this with Eq. 12, we recognize that

$$\langle\alpha\rangle=\left.\frac{d\tau(q)}{dq}\right|_{q=0}\ . \qquad (15)$$

From Eq. (7b), we see that this is also $\alpha(q=0)$, which we will denote by α_0 from here on. Taking the second derivative of $G(q)$, one can similarly show that

$$\left.\frac{d^2G(q)}{dq^2}\right|_{q=0}=[\ln(r/L)]^2\langle\alpha^2\rangle$$
$$=[\ln(r/L)]^2\{[\ln(r/L)]^{-1}d^2\tau/dq^2+(d\tau/dq)^2\}_{q=0}\ . \qquad (16)$$

From this it follows that σ_α^2, the variance of α, is given by

$$\sigma_\alpha^2=\langle(\alpha-\alpha_0)^2\rangle=[\ln(r/L)]^{-1}\left.\frac{d^2\tau(q)}{dq^2}\right|_{q=0}\ . \qquad (17)$$

Thus, for multifractals, the variance of the variable α is a function of r, and decreases as r decreases. As a matter of future convenience, we now focus on the variance $\sigma_{\ln p}^2$ of $\ln(p_r)$. Since $\ln(p_r)\sim\alpha\ln(r/L)$ from Eq. (1), we obtain

$$\sigma_{\ln p}^2=-\left.\frac{d^2\tau(q)}{dq^2}\right|_{q=0}\ln(L/r)\ . \qquad (18)$$

Therefore, for multifractal measures, the variance of the logarithm of the measure in a box of size r increases with decreasing box size. It is convenient to define an intermittency exponent μ according to[22]

$$\mu=-\left.\frac{d^2\tau(q)}{dq^2}\right|_{q=0}\ . \qquad (19)$$

Taking the derivative of $G(q)$ to order n, it is easy to show that the nth centered moment of α is given in terms of $\tau(q)$ and the box size r as

$$\langle(\alpha-\alpha_0)^n\rangle=[\ln(r/L)]^{1-n}\left.\frac{d^n\tau(q)}{dq^n}\right|_{q=0}\ . \qquad (20)$$

One can again define generalized intermittency exponents of order n, μ_n, according to

$$\mu_n=-\left.\frac{d^n\tau(q)}{dq^n}\right|_{q=0}\ . \qquad (21)$$

The next chapter is devoted to a generalization of these ideas to multivariate distributions.

III. JOINT MULTIFRACTAL DISTRIBUTIONS: THEORY

As outlined in the Introduction, it is of interest to characterize jointly the distributions and properties of several multifractal measures coexisting in the same spatial region. Our interest in such a problem stems from the realization that in turbulent flows, there exist distinct multifractal measures embedded in the flow field. For instance, the dissipation of turbulent kinetic energy ε, the dissipation of passive scalar fluctuations χ when a scalar is advected by the flow, the magnitude of the vorticity field, etc. There exist other situations in physics where several multifractal measures of interest coexist in the same region. For instance, in problems of diffusion limited aggregation, both the growth probability distribution and the harmonic measure are believed to be multifractals, both lying on the boundary of the aggregate. (It is expected that both are the same at any point, and a way to check this would be to measure their joint distribution.)

For notational simplicity, the treatment will be done for bivariate distributions, but extension of these ideas to more than two multifractal distributions is trivial. Section III A introduces the concept of joint multifractal spectra and Sec. III B focuses on joint moment exponents. In Sec. III C, we describe the application of μ-weighted averaging for obtaining the joint multifractal spectrum. Section III D introduces the intermittency and correlation exponents for joint multifractals.

A. Joint multifractal spectra

The situation we have in mind is that of two distinct multifractal measures coexisting in the same spatial domain. As usual, we divide the domain into boxes of size r and define $p_r(x_i)$ and $p'_r(x_i)$ as the integrated measures in such boxes centered around the position x_i. From here on, the superscript prime is used to distinguish one measure from the other. We then define two local singularity strengths α, and α', according to

$$p_r(x_i)\sim(r/L)^{\alpha} \tag{22a}$$

and

$$p'_r(x_i)\sim(r/L)^{\alpha'} , \tag{22b}$$

and focus on the joint distributions of the variables α and α'. $N_r(\alpha,\alpha')d\alpha\, d\alpha'$ will denote the number of boxes of size r in which the variable α has values in a band $d\alpha$ around α, and α' in a band $d\alpha'$ around α'. In analogy to the usual multifractal formalism, it is convenient to define $f(\alpha,\alpha')$ as the scaling exponent of $N_r(\alpha,\alpha')$ according to

$$N_r(\alpha,\alpha')d\alpha\, d\alpha'\sim(r/L)^{-f(\alpha,\alpha')}d\alpha\, d\alpha' . \tag{23}$$

From a geometrical point of view, Eq. (23) has the following meaning. If we concentrate on a set of boxes of size r where α has a certain value, and α' has another given value, then $f(\alpha,\alpha')$ is the fractal dimension of this set. Another way of expressing this is to say that $f(\alpha,\alpha')$ is the dimension of a set resulting from the intersection of an iso-α and iso-α' set.

The curve $f(\alpha,\alpha')$ will therefore characterize the scaling properties of the joint distribution of the local exponents α and α'. Thus the multifractal formalism is extended to more than one measure.[23]

B. Joint moment exponents

Consider joint moments of the form $\langle[p_r(x_i)]^q[p'_r(x_i)]^p\rangle$ or, alternatively, sums of the form $\sum_i[p_r(x_i)]^q[p'_r(x_i)]^p$. The joint moment exponent $\tau(q,p)$ is defined according to

$$\sum_i(p_r(x_i)]^q[p'_r(x_i)]^p\sim(r/L)^{\tau(q,p)} . \tag{24}$$

The sum is performed over all boxes (one uses $0^0=0$). The scaling exponent $\tau(q,p)$ is analogous to $\tau(q)$ for the case of a single multifractal. The parameters q and p have the following meaning. For high positive values of q and p, $\tau(q,p)$ characterizes the scaling behavior of regions where both measures are very intense. Large negative values of q and p focus on regions where both measures are very sparse. Large positive q and large negative p emphasize regions where the first measure is very intense, but the second measure is very sparse, and vice versa.

If D_q and D'_p are the moment exponents for individual measures, we have as special cases of Eq. (24) that

$$\sum_i[p_r(x_i)]^q[p'_r(x_i)]^{p=0}\sim(r/L)^{(q-1)D_q} , \tag{25a}$$

$$\sum_i[p_r(x_i)]^{q=0}[p'_r(x_i)]^p\sim(r/L)^{(p-1)D'_p} , \tag{25b}$$

or

$$\tau(q,0)=(q-1)D_q , \tag{26a}$$

$$\tau(0,p)=(p-1)D'_p . \tag{26b}$$

We can in principle obtain $\tau(q,p)$ by computing $\sum_i p_r(x_i)^q p'_r(x_i)^p$ for a variety of box sizes r and also as the slope of plots of $\ln\{\sum_i[p_r(x_i)]^q[p'_r(x_i)]^p\}$ vs $\ln(r/L)$.

The next question concerns the relation between the exponents $\tau(q,p)$ and the joint-distribution exponent $f(\alpha,\alpha')$. For this purpose, one writes the sum of Eq. (24) as a double integral over all values of α and α' according to

$$\sum_i[p_r(x_i)]^q[p'_r(x_i)]^p\sim\sum_i(r/L)^{\alpha q+\alpha' p}\sim\int\int(r/L)^{\sigma(\alpha,\alpha')}d\alpha\, d\alpha' , \tag{27a}$$

where

$$\sigma(\alpha,\alpha')=\alpha q+\alpha' p-f(\alpha,\alpha') . \tag{27b}$$

At this point, we apply the method of steepest descent to evaluate the integral at small values of r. Therefore

$$\sum_i p_r^q(p'_r)^p\sim r^{\alpha q+\alpha' p-f(\alpha,\alpha')} \tag{28}$$

or

$$\tau(q,p)=\alpha q+\alpha' p-f(\alpha,\alpha') , \tag{29}$$

where α and α' are given by the conditions

$$\frac{\partial f(\alpha,\alpha')}{\partial\alpha}=q \tag{30a}$$

$$\frac{\partial f(\alpha,\alpha')}{\partial\alpha'}=p . \tag{30b}$$

Taking partial derivatives of Eq. (29) with respect to q in order to invert the transform, one obtains

$$\frac{\partial\tau(q,p)}{\partial q}=\alpha+q\frac{\partial\alpha}{\partial q}-\frac{\partial f}{\partial\alpha}\frac{\partial\alpha}{\partial q}+p\frac{\partial\alpha'}{\partial q}-\frac{\partial f}{\partial\alpha'}\frac{\partial\alpha'}{\partial q} . \tag{31}$$

But using $\partial f/\partial\alpha=q$ and $\partial f/\partial\alpha'=p$, and repeating the same procedure for p and α', we obtain the double Legendre transforms that relate the triads (τ,q,p) with (f,α,α') as

$$\alpha(q,p)=\partial\tau(q,p)/\partial q , \tag{32a}$$

$$\alpha'(q,p)=\partial\tau(q,p)/\partial p , \tag{32b}$$

$$f(\alpha,\alpha')=\alpha(q,p)q+\alpha'(q,p)p-\tau(q,p) . \tag{32c}$$

Given the function $\tau(q,p)$, one can therefore obtain the distribution function $f(\alpha,\alpha')$, and vice versa.

C. Obtaining $f(\alpha,\alpha')$ using the method of μ-weighted averaging

We will not attempt to measure $f(\alpha,\alpha')$ by directly analyzing the scaling properties of joint histograms $N_r(\alpha,\alpha')$ that could be constructed from both measures. The reason, as described in Ref. 18, is that the results

would suffer from logarithmic corrections if applied to experimental data with a limited scaling range. Instead, we obtain $f(\alpha,\alpha')$ directly by implementing the method of μ-weighted averaging for joint multifractal measures.

To this effect, we first note that we have two control parameters q and p. Their role was explained in the last section. Define a new normalized μ measure, which depends on the box size r, and on both p and q, according to

$$\mu_r(x_i;q,p)=\frac{[p_r(x_i)]^q[p_r'(x_i)]^p}{\sum_i[p_r(x_i)]^q[p_r'(x_i)]^p} . \tag{33}$$

The average value of $\alpha=\ln[p_r(x_i)]/\ln(r/L)$ with respect to this μ-measure will be given by

$$\alpha(q,p)=\sum_i\{\mu_r(x_i;q,p)\ln[p_r(x_i)]\}/\ln(r/L) . \tag{34a}$$

Similarly, the scaling exponent $\alpha'(q,p)$ of the second measure will be given in terms of the average value of $\alpha'=\ln[p_r(x_i)]/\ln(r/L)$ according to

$$\alpha'(q,p)=\sum_i\{\mu_r(x_i;q,p)\ln[p_r'(x_i)]\}/\ln(r/L) . \tag{34b}$$

Therefore, one can argue that the μ-measure $\mu_r(x_i;q,p)$ "highlights" a particular set on which $\alpha=\alpha(q,p)$ and $\alpha'=\alpha'(q,p)$ are the mean values of the local singularity strengths. Again, the dimension of the measure-theoretic support of $\mu_r(x_i;q,p)$ is given by

$$\dim[\mu_r(x_i;q,p)]=\lim_{r\to 0}\frac{\sum_i\{\mu_r(x_i;q,p)\ln[\mu_r(x_i;q,p)]\}}{\ln(r/L)} . \tag{35}$$

$\mathrm{Dim}[\mu_r(x_i;q,p)]$ is therefore the dimension of a set on which $\alpha(q,p)$ and $\alpha'(q,p)$ are the mean local exponents of both measures. By simple manipulations, it is easy to show that $\dim[\mu_r(x_i;q,p)]$ corresponds to $f(\alpha,\alpha')$ as defined in Eq. (7a). Thus, we have extended the method of μ-weighted averaging to joint multifractal distributions. One can now measure α and α' from plots of $\sum_i\{\mu_r(x_i;q,p)\ln[p_r(x_i)]\}$ and $\sum_i\{\mu_r(x_i;q,p)\ln[p_r'(x_i)]\}$ vs $\ln(r/L)$, and $f(\alpha,\alpha')$ from plots of $\sum_i\{\mu_r(x_i;q,p)\ln[\mu_r(x_i;q,p)]\}$ vs $\ln(r/L)$. Different pairs of (α,α') are scanned by tuning the parameters (q,p).

D. Definition of intermittency and correlation exponents

Let us now define a bivariate generating function $G(q,p)$ according to

$$G(q,p)=\int\int(r/L)^{\alpha q+\alpha' p-f(\alpha,\alpha')+D_0}d\alpha\,d\alpha' . \tag{36}$$

Evaluating the partial derivatives of $G(q,p)$ at the origin, the following results are obtained:

$$\langle(\alpha-\alpha_0)^2\rangle=[\ln(r/L)]^{-1}\frac{\partial^2\tau(q,p)}{\partial q^2}\bigg|_{q=p=0} , \tag{37a}$$

$$\langle(\alpha'-\alpha_0')^2\rangle=[\ln(r/L)]^{-1}\frac{\partial^2\tau(q,p)}{\partial p^2}\bigg|_{q=p=0} . \tag{37b}$$

The individual intermittency exponents of both measures can therefore be obtained by

$$\mu=-\partial^2\tau(q,p)/\partial q^2\big|_{q=p=0} . \tag{38a}$$

$$\mu'=-\partial^2\tau(q,p)/\partial p^2\big|_{q=p=0} . \tag{38b}$$

Next, it is of interest to compute ρ, the correlation coefficient between α and α' defined as

$$\rho=\frac{\langle(\alpha-\alpha_0)(\alpha'-\alpha_0')\rangle}{\langle(\alpha-\alpha_0)^2\rangle^{1/2}\langle(\alpha'-\alpha_0')^2\rangle^{1/2}} \tag{39}$$

Taking mixed derivatives of $G(q,p)$ one obtains the following general expression for ρ:

$$\rho=\frac{-\dfrac{\partial^2\tau}{\partial p\,\partial q}}{\left[\dfrac{\partial^2\tau}{\partial q^2}\dfrac{\partial^2\tau}{\partial p^2}\right]^{1/2}}\Bigg|_{q=p=0}=\frac{-\dfrac{\partial^2\tau}{\partial q\,\partial p}}{\left[\dfrac{\partial^2\tau}{\partial q^2}\dfrac{\partial^2\tau}{\partial p^2}\right]^{1/2}}\Bigg|_{q=p=0} \tag{40}$$

This is also the correlation coefficient between $\ln[p_r(x_i)]$ and $\ln[p_r'(x_i)]$.

It is clear that such a formulation can be carried further to N joint-multifractal measures. For such cases, one obtains a joint moment exponent $\tau(q_1,q_2,\ldots,q_N)$, and the second-order statistics of the local scaling exponents $\alpha^{(1)},\alpha^{(2)},\ldots,\alpha^{(N)}$ can be described by a covariance matrix defined according to $\mu_{ij}=-\partial^2\tau(q_1,q_2,\ldots,q_N)/\partial q_i\partial q_j$.

E. Statistical dependence and independence

In this section we analyze two limiting cases, where the two measures are either independent or entirely dependent.

1. *Independent distributions*

When $p_r(x_i)$ and $p_r'(x_i)$ are independent, one can write that

$$\sum_i[p_r(x_i)]^q[p_r'(x_i)]^p\sim r^{-d}\langle[p_r(x_i)]^q[p_r'(x_i)]^p\rangle$$
$$=r^{-d}\langle[p_r(x_i)]^q\rangle\langle[p_r'(x_i)]^p\rangle . \tag{41}$$

Therefore, $\tau(q,p)$ of independent multifractals is

$$\tau(q,p)=d+(q-1)D_q+(p-1)D_p' . \tag{42}$$

From this it follows directly [applying Eqs. (7)] that

$$f(\alpha,\alpha')=f(\alpha)+f(\alpha')-d . \tag{43}$$

This can also be obtained by realizing that the probability of an iso-(α,α') set is the product of the individual independent probabilities of finding an iso-α set and an iso-α' set. Therefore,

$$\Pi_r(\alpha,\alpha')\sim(r/L)^{d-f(\alpha,\alpha')}\sim\Pi_r(\alpha)\Pi_r(\alpha')\sim r^{2d-f(\alpha)-f(\alpha')}, \tag{44}$$

from which (43) follows directly.

2. Completely dependent distributions

In such cases, when α has a certain value, α' has always the same value. Therefore, there is a one-to-one relation between α and α', which we write as $\alpha'=\alpha'(\alpha)$. Now,

$$\sum_i [p_r(x_i)]^q [p_r'(x_i)]^p \sim (r/L)^{q\alpha+p\alpha'(\alpha)-f(\alpha)} , \tag{45}$$

where α is the solution to

$$\frac{\partial f(\alpha)}{\partial \alpha} = q + p\frac{\partial \alpha'}{\partial \alpha} . \tag{46}$$

Of course, this should be equal to the results that one obtains by expressing α as a function of α':

$$\sum_i [p_r(x_i)]^q [p_r'(x_i)]^p \sim (r/L)^{q\alpha(\alpha')+p\alpha'-f'(\alpha')} , \tag{47}$$

where α' is the solution to

$$\frac{\partial f'(\alpha')}{\partial \alpha'} = p + q\frac{\partial \alpha}{\partial \alpha'} . \tag{48}$$

Therefore, $\tau(q,p)$ for completely dependent joint multifractals is

$$\tau(q,p)=q\alpha+p\alpha'(\alpha)-f(\alpha)=p\alpha'+q\alpha(\alpha')-f'(\alpha') , \tag{49}$$

where α in the first equality is given by the solution to Eq. (46) and α' in the second equality is given by the solution to Eq. (48).

IV. TWO SPECIAL CASES

In this Section, we analyze joint log-normal and joint binomial distributions. Log-normality is traditionally believed to be a reasonable approximation of the distribution of small-scale quantities in turbulence, whereas binomial models arise naturally in describing cascade models.[11]

A. Joint log-normal distributions

If both measures are formed by multiplicative processes, the variables $\ln[p_r(x_i)]$ and $\ln[p_r'(x_i)]$ are each given by the sum of the logarithm of some multipliers. The central-limit theorem would then suggest that both variables $p_r(x_i)$ and $p_r'(x_i)$ form a joint log-normal distribution. The purpose of this section is to elaborate on the properties of joint log-normal distributions. However, for general multifractals, we expect log-normality to be a good approximation only around the maximum of the distribution, and not near its tails.[24,9,8]

The probability density function of two joint log-normal variables p_r and p_r' has the form

$$\Pi(p_r,p_r') = (2\pi p_r p_r' \sigma\sigma')^{-1} \exp(\phi) , \tag{50a}$$

where

$$\phi = [2(1-\rho^2)]^{-1}\{[\ln(p_r)-m]^2/\sigma^2 - 2\rho[\ln(p_r)-m][\ln(p_r')-m']/\sigma\sigma' + [\ln(p_r')-m']^2/\sigma'^2\} . \tag{50b}$$

Here, m,m' and σ^2,σ'^2 are, respectively, the means and variances of $\ln(p_r)$ and $\ln(p_r')$, ρ being their correlation coefficient. From Sec. II, we know that these values are given by

$$m = \alpha_0 \ln(r/L) , \tag{50c}$$

$$m' = \alpha_0' \ln(r/L) , \tag{50d}$$

$$\sigma^2 = \mu \ln(L/r) , \tag{50e}$$

$$\sigma'^2 = \mu' \ln(L/r) . \tag{50f}$$

Here μ and μ' are the intermittency exponents of each of the individual log-normal measures. This type of distribution was proposed by Van Atta[25] for describing the joint distribution of the dissipation of kinetic energy and passive scalar variance.

Using $p_r(x_i)\sim r^{\alpha}$ and $p_r'(x_i)\sim r^{\alpha'}$ and recalling that $\Pi_r(\alpha,\alpha')\sim r^{d-f(\alpha,\alpha')}$, we obtain that $f(\alpha,\alpha')$ of joint log-normal distributions is given by

$$f(\alpha,\alpha') = d - [2(1-\rho^2)]^{-1} \times [(\alpha-\alpha_0)^2/\mu - 2\rho(\alpha-\alpha_0)(\alpha'-\alpha_0')/(\mu\mu')^{1/2} + (\alpha'-\alpha_0')/\mu'] . \tag{51}$$

This is an elliptic paraboloid, whose eccentricity and inclination are controlled by the correlation coefficient ρ.

Applying relations (32), we can obtain α, α', and $f(\alpha,\alpha')$ as functions of parameters q and p. The results are

$$\alpha(q,p) = d + \mu/2 - [\mu q + \rho(\mu\mu')^{1/2} p] , \tag{52a}$$

$$\alpha'(q,p) = d + \mu'/2 - [\mu' p + \rho(\mu\mu')^{1/2} q] , \tag{52b}$$

$$f(\alpha,\alpha') = d - [\mu q^2 + 2\rho(\mu\mu')^{1/2} qp + \mu' p^2]/2 . \tag{52c}$$

Finally, $\tau(q,p)$ for joint log-normal measures is

$$\tau(q,p) = (q+p-1)d + (q\mu+p\mu')/2 - [\mu q^2 + 2\rho(\mu\mu')^{1/2} qp + \mu' p^2]/2 . \tag{52d}$$

Notice that for a multivariate log-normal, the scaling exponent of the joint distribution can be written as

$$f(\alpha^{(1)},\alpha^{(2)},\ldots,\alpha^{(N)}) = d - \tfrac{1}{2}(\alpha^{(i)}-\alpha_0^{(i)})\mu_{ij}^{-1}(\alpha^{(j)}-\alpha_0^{(j)}] , \tag{53}$$

where μ^{-1} is the inverse of the covariance matrix of the local exponents $\alpha^{(i)}$.

B. Joint binomial multifractal measures

A joint binomial cascade produces two distinct binomial measures defined on the same unit interval. It proceeds as follows: One starts with two uniform distributions defined on the unit interval. At the first iteration ($n=1$), the unit interval is split into two equal pieces of length $\frac{1}{2}$. The total measure of both distributions is now multiplied by multipliers M and M' (the prime again distinguishes between the two distributions), where M and

M' are random numbers selected according to some rule. This then determines the new values of both measures on each of the two pieces. At the second iteration ($n=2$), both pieces divide again into equal pieces of size $\frac{1}{4}$, and for each piece a random choice for both M and M' is made, according to the same rule as before. After many steps, two distinct multifractal measures are generated on the same unit interval.

The simplest nontrivial choice for this process is to select M and M' from a binomial distribution. For instance, $M=p_1$ or $p_2=1-p_1$ with equal probability, and $M'=p'_1$ or $p'_2=1-p'_1$ also with equal probability (say $p_1>\frac{1}{2}$ and $p'_1>\frac{1}{2}$). There are now several possibilities concerning the degree of correlation of the multipliers M and M' at each piece. If the two multipliers are selected in a completely independent manner, both measures will be independent joint multifractals (see Sec. III E 1). On the other hand, if every time a piece receives for the first distribution a multiplier $M=p_1$, it receives for the other distribution the multiplier $M'=p'_1$ (or whenever $M=p_2$ then $M'=p'_2$), then the two resulting multifractal measures are completely dependent (see Sec. III E 2). Completely anticorrelated measures would result if $M=p_1$ whenever $M'=p'_2$, and $M=p_2$ whenever $M'=p'_1$.

A plethora of intermediate possibilities exists in terms of the degree of correlation between the two processes. For illustrative purposes, we will focus on two cases. The first one consists of a process where with probability γ both multipliers M and M' are completely dependent, and with probability $1-\gamma$ they are anticorrelated. We now compute $\tau(q,p)$ of such a joint binomial distribution.

In general, each $p(x_i)$ and $p'_r(x_i)$ will be given by the product of n realizations of the multipliers M and M'. Therefore

$$\sum_i [p_r(x_i)]^q [p'_r(x_i)]^p \sim r^{-1} \langle [p_r(x_i)]^q [p'_r(x_i)]^p \rangle \sim r^{-1} \left\langle \prod_{i=1}^{n} M_i^q (M'_i)^p \right\rangle . \quad (54)$$

The averaging is performed over all boxes. One can also compute the average of $\sum_i [p_r(x_i)]^q [p'_r(x_i)]^p$ over the entire distribution of M and M'. If we assume that there are no correlations between the cascade steps at different levels, we can write

$$\sum_i [p_r(x_i)]^q [p'_r(x_i)]^p \sim r^{-1} \langle M^q M'^p \rangle^n . \quad (55)$$

One can now write

$$\langle M^q M'^p \rangle = \gamma \langle M^q M'^p \rangle_{\text{corr}} + (1-\gamma) \langle M^q M'^p \rangle_{\text{anticorr}} . \quad (56)$$

Now we recall that M can take values p_1 and p_2 (with equal probability), and M' can take values p'_1 and p'_2. In such a case the moments are given by

$$\langle M^q M'^p \rangle_{\text{corr}} = [p_1^q (p'_1)^p + p_2^q (p'_2)^p]/2 , \quad (57a)$$

$$\langle M^q M'^p \rangle_{\text{anticorr}} = [(p_1^q (p'_2)^p + p_2^q (p'_1)^p]/2 . \quad (57b)$$

Substituting these values in Eq. (56) and using $r=2^{-n}$, we obtain $\tau(q,p)$ for such a joint distribution as

$$\tau(q,p) = -\log_2 \{ \gamma [p_1^q (p'_1)^p + p_2^q (p'_2)^p] + (1-\gamma)[p_1^q (p'_2)^p + p_2^q (p'_1)^p] \} . \quad (58)$$

To compute the intermittency and correlation exponents, we evaluate derivatives of $\tau(q,p)$ at $q=p=0$ to obtain

$$\mu = -\left. \frac{\partial^2 \tau}{\partial q^2} \right|_{0,0} = \ln(p_1/p_2)\ln(p_1/p_2)/(4\ln 2) , \quad (59a)$$

$$\mu' = -\left. \frac{\partial^2 \tau}{\partial p^2} \right|_{0,0} = \ln(p'_1/p'_2)\ln(p'_1/p'_2)/(4\ln 2) , \quad (59b)$$

$$\left. \frac{\partial^2 \tau}{\partial p \, \partial q} \right|_{0,0} = (1-2\gamma)\ln(p_1/p_2)\ln(p'_1/p'_2)/(4\ln 2) . \quad (59c)$$

Therefore, using the definition of ρ [Eq. (40)], we obtain

$$\rho = 2\gamma - 1 . \quad (60)$$

This is consistent with the expected behavior of ρ as a function of γ.

If one assumes, as the second example, that the two processes are completely correlated with probability γ, while being completely independent with probability $(1-\gamma)$, one can show that $\tau(q,p)$ is now given by

$$\tau(q,p) = -\log_2 \{ \gamma (p_1^q + p_2^q) + (1-\gamma)/2 [(p'_1)^p + (p'_2)^p] \times [p_1^q (p'_1)^p + p_2^q (p'_2)^p] \} . \quad (61)$$

The individual intermittency exponents are the same as before, but the correlation exponent ρ turns out to be

$$\rho = \gamma . \quad (62)$$

Both Eqs. (61) and (58) give the same result when expressed in terms of ρ: namely,

$$\tau(q,p) = -\log_2 \{ \rho (p_1^q + p_2^q) + (1-\rho)/2 [(p'_1)^p + (p'_2)^p] \times [p_1^q (p'_1)^p + p_2^q (p'_2)^p] \} . \quad (63)$$

It appears at this level of description that the details of how precisely the partial degree of correlation comes about is immaterial. We will return to joint binomial models after analyzing experimental results in the next section.

V. JOINT MULTIFRACTAL DISTRIBUTION OF $(\partial u_1/\partial x)^2$ AND $(\partial T/\partial x)^2$

In turbulent flows, it is usually thought that some cascade process[26,27] is responsible for the transfer of kinetic energy from the large scales to the small scales of motion. The cascade ends at the smallest scale of motion, the Kolmogorov scale η, at which the flux of kinetic energy to smaller scales equals the dissipation ε, defined as

$$\varepsilon(\mathbf{x},t) = \frac{\nu}{2} \left[\frac{\partial u_i}{\partial x_j} + \frac{\partial u_j}{\partial x_i} \right]^2 . \quad (64a)$$

Here ν is the kinematic viscosity of the fluid, and the u_i's are the instantaneous turbulent velocity components. If the turbulent flow is advecting a passive scalar of concen-

tration θ, then there is also a flux of the scalar variance to smaller scales.[27,28] At the smallest scales it is equal to χ, the rate of dissipation of passive scalar fluctuations, defined as

$$\chi(\mathbf{x},t)=\Gamma\left[\frac{\partial\theta}{\partial x_i}\right]^2 . \tag{64b}$$

Γ is the molecular diffusivity of the scalar θ. Such cascade processes generically produce very intermittent distributions of dissipation, a well known feature of small scale turbulence. As mentioned already, both ε and χ have been shown individually to be multifractals. This section is devoted to the study of their joint distribution. For experimental reasons, we can only study the joint distribution of single terms of Eqs. (64). This means that we will only consider surrogates ε' and χ' of dissipation, defined as

$$\varepsilon'=\left[\frac{\partial u_1}{\partial x}\right]^2 , \tag{65a}$$

and

$$\chi'=\left[\frac{\partial\theta}{\partial x}\right]^2 , \tag{65b}$$

where u_1 is the streamwise velocity component, and x is the streamwise coordinate. For the scalar, we use heat; θ is then the fluctuating temperature T.

Joint measurements of velocity and temperature were performed by Antonia and Van Atta[29] in a heated jet. Using Taylor's hypothesis they measured a correlation coefficient between $\ln(\partial u_1/\partial x)^2$ and $\ln(\partial T/\partial x)^2$ of the order of 0.5. Similar measurements were made by Antonia and Chambers[30] in the atmospheric surface layer. They obtained slightly lower estimates for the correlation coefficient.

The aim of the present section is to make similar measurements in the turbulent wake of a heated cylinder, and to measure the entire joint distribution of ε' and χ'. We expect a joint multifractal distribution, and analyze appropriate experimental results using the theory outlined in Sec. III. In Sec. V A we present the experimental procedure. Section V B explains data processing and Sec. V C presents the results. Section V D contains a comparison of the present results with the previous ones on structure functions of temperature; we also present some modeling ideas using joint binomial measures.

A. Experimental procedure

Joint measurements of velocity and temperature were performed in the wake of a heated cylinder. The temperature fluctuations were measured with a 0.6-μm-diameter cold wire, operated at a constant current of 120 μA. The cold-wire electronics was based on the design by Peattie.[31] The velocity fluctuations were measured using a 5-μm diam hot wire, operated at an overheat of 1.7 on a DANTEC 55M10 constant-temperature bridge. Both the sensors were made of Pt–10% Rh. The actual lengths of both the sensors was 0.5 mm. The free stream velocity was 9 m/s and the rise of mean temperature above the ambient was 2.5 °C. The cylinder diameter D was 1.9 cm, so that the Reynolds number based on it is about 12 000. The measuring station was at $x/D=90$ from the cylinder at the fluid dynamic centerline. The cylinder was heated uniformly with internal heating elements. Forty files of 1.2×10^5 data points were taken using two-channel data acquisition. The signal from the cold wire was filtered at 4.0 kHz, and that from the hot wire at 6.3 kHz, using two DANTEC 55D26 signal conditioners. The signals were sampled at a data acquisition frequency of 15 kHz on a 12-bit analog-to-digital (AD) converter of a MASSCOMP 5500 computer. The Kolmogorov scale was estimated to be of the order of $\eta\approx0.03$ cm, the integral scale computed from the autocorrelation of the velocity signal was 7 cm, and the first zero crossing of the autocorrelation function occurred at around 25 cm.

One of the most important considerations in operating the hot and cold wires simultaneously is that the two wires must in principle be as close together as possible, but yet there must be minimum interference between them. In principle, the distance between the two probes needs to be closer than a Kolmogorov scale but, in such closeness, the hot wire, which operates at temperatures of the order of a few hundred degrees, tends to contaminate the cold-wire signals. Much effort was invested on this issue, and details will be reported elsewhere. The net result is that an optimal configuration was arrived at by placing the cold wire 0.5 mm upstream of the hot wire and at right angles to it, so that the upstream-downstream view was a cross. This configuration practically eliminates thermal effects of the hot wire on the cold wire. A further discussion of this point is given in Sec. V C.

The quantities ε' and χ' were obtained by simply differencing the velocity and the temperature signals according to

$$\varepsilon'\sim\left[\frac{\partial u_1}{\partial t}\right]^2\sim[u_1(t+\delta t)-u_1(t)]^2 , \tag{66a}$$

$$\chi'\sim\left[\frac{\partial T}{\partial t}\right]^2\sim[T(t+\delta t)-T(t)]^2 , \tag{66b}$$

where δt was the sampling interval corresponding approximately to two Kolmogorov time scales. Here we use Taylor's frozen flow hypothesis. The use of Taylor's hypothesis for this purpose has been partially substantiated by the results of Refs. 13, 14, and 32. In subsequent stages of data processing, ε' and χ' will be normalized, so that we need not worry about numerical prefactors in Eqs. (66). As already noted, Figs. 1(a) and 1(b) show typical segment of data of ε' and χ' along the *same* linear cut. It appears from these typical data segments that no strong correlation exists between the intense peaks of these two signals. The actual correlation will be quantified more rigorously in the following sections. Clearly, ε' is less intermittent than χ'.

Now let us divide the entire data set into disjoint "boxes" of size r. We define $E_r(x_i)$ and $X_r(x_i)$ as the total ε' and χ' contained in a box of size r centered at position x_i, normalized by the total dissipation on the entire data set of length L considered. L is much larger than the integral scale. That is,

$$E_r(x_i)=\frac{\int_{x_i-r/2}^{x_i+r/2}\varepsilon'(x')dx'}{\int_0^L\varepsilon'(x')dx'}\ , \tag{67}$$

$$X_r(x_i)=\frac{\int_{x_i-r/2}^{x_i+r/2}\chi'(x')dx'}{\int_0^L\chi'(x')dx'}\ . \tag{68}$$

If ε' and χ' form a joint multifractal distribution, we expect that

$$E_r(x)\sim r^{\alpha} \tag{69}$$

$$X_r(x)\sim r^{\alpha'}\ , \tag{70}$$

$$N_r(\alpha,\alpha')\sim r^{-f(\alpha,\alpha')}\ , \tag{71}$$

in addition to

$$\sum_i [E_r(x_i)]^q[X_r(x_i)]^p\sim r^{\tau(q,p)}\ . \tag{72}$$

Here $\sim$ means "proportional to" (the prefactors in these relations may differ greatly from unity). The sum in Eq. (72) is performed over all (disjoint) boxes of size r.

B. Processing the data

We are now interested in evaluating the following sums over all boxes of size r contained in the data set of length L:

$$\sum_i \mu_r(x_i;q,p)\ln[E_r(x_i)]\ , \tag{73}$$

$$\sum_i \mu_r(x_i;q,p)\ln[X_r(x_i)]\ , \tag{74}$$

$$\sum_i \mu_r(x_i;q,p)\ln[\mu_r(x_i;q,p)]\ , \tag{75}$$

$$\ln\left[\sum_i [E_r(x_i)]^q[X_r(x_i)]^p\right]\ , \tag{76}$$

where

$$\mu_r(x_i;q,p)=[E_r(x_i)]^q[X_r(x_i)]^p\Big/\sum_i [E_r(x_i)]^q[X_r(x_i)]^p\ . \tag{77}$$

In Ref. 9, the basic observation was made that if L was chosen to be very large in order to guarantee the convergence of moments, the extent of the power-law regimes was consistently shorter than if L was chosen to be of the order of 30 integral scales or so. (We point out that in many cases the scaling range is larger than the usual inertial range, but this needs better quantification.) The issue is documented in detail in Ref. 12. For completeness, we present both procedures of measuring the scaling exponents. In the first method, the quantities of Eqs. (73)–(77) are obtained by using $L=4.3\times10^4$ times the integral scale, that is, we use all 5×10^6 data points available from the measurements. Here it is of interest to study the speed of convergence of moments. To show that the number of data points considered here is sufficient to guarantee such a convergence, it is best to plot moments of the form $\langle\varepsilon_r^q\chi_r^p\rangle$ as a function of the number of data points used to compute the averages. Here ε_r and χ_r are the dissipation rates averaged in a box of size r, or $\varepsilon_r=E_r/r$, $\chi_r=X_r/r$. This is done for different box sizes r. The results are shown in Figs. 2(a)–(d) for different choices of q and p. For convenience, we plot the (normalized) results in logarithmic units, and divide by $(q+p-1)$. As can be seen, after 5×10^6 points, the convergence is good (especially for box sizes $r/\eta\geq30$), even for moments of order as high as $p+q=8$.

In the second method, we obtain the sums of Eqs. (73)–(77) using $L=40$ times the integral scale, that is, we use 5×10^3 data points only. This is then repeated for 20 such segments of data.

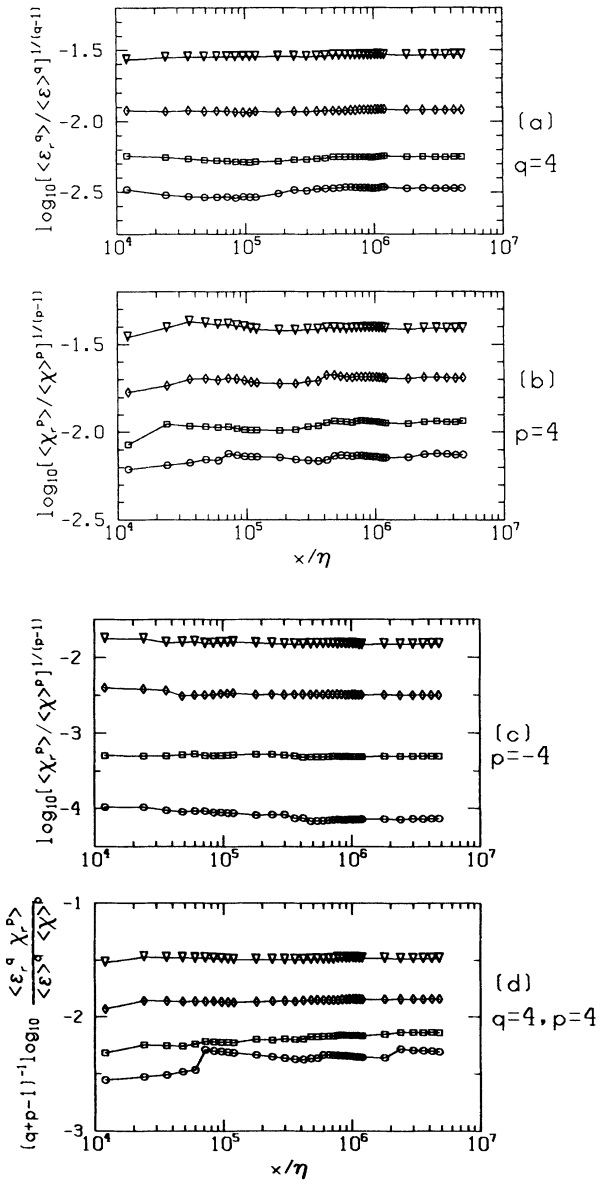

FIG. 2. Convergence of moments as a function of the length of the data. Different symbols correspond to different box sizes r. Circles, $r/\eta=10$; squares, $r/\eta=30$; diamonds, $r/\eta=100$; triangles, $r/\eta=300$. (a) shows the convergence of the fourth moments of ε_r. (b) shows the same for χ_r. In (c), we show the convergence of the fourth negative moment of χ_r, and (d) is for a mixed moment of order 8 ($q=4$, $p=4$).

The calculation of the quantities in (73)–(77) is repeated for a variety of values of q and p. A total of 17^2 pairs of (q,p) are used, equally spaced at the interval of 0.5 between -4 and $+4$. Twenty-four different box sizes between $r/\eta=5$ and $r/\eta=1000$ are used. We then obtain the exponents $\alpha(q,p)$, $\alpha'(p,q)$, $f(q,p)$, and $\tau(q,p)$ from the slopes of plots of the computed quantities as a function of the box size. Figures 3(a)–3(d) show such plots for the method of long-term averaging. $\alpha(q,p)$ is obtained from plots such as Fig. 3(a), α' (q,p) from Fig. 3(b), $f(\alpha,\alpha')$ from 3(c) and $\tau(q,p)$ from plots such as 3(d). Notice that for convenient representation, we plot

$$\ln[\sum_i [E_r(x_i)]^q X_r(x_i)]^p]^{1/(q+p-1)}$$

instead of expression (76), so that the slopes shown in Fig. 3(d) correspond to $\tau(q,p)/(q+p-1)$ rather than to $\tau(q,p)$.

Representative samples of the relevant plots for the method of short-term averaging are presented in the Appendix.

The slopes are obtained by least-square error fits through the points within a range of scales in which the graphs appear most linear. As can be seen in Fig. 3, for the long-term averaging procedure such a range is unambiguous (1.5 decades) for the expressions involving χ' only, the dissipation of the scalar (this is, when q is close to zero). However, the plots involving ε' only (where p is close to zero) seem to possess shorter linear segments. Thus it seems that χ' possesses a larger range of self-similarity than does ε'. It is not entirely clear why this must be so, but one possible reason is that χ' represents the scalar dissipation more accurately than ε' does ε because, unlike ε, χ does not contain any cross terms [see Eqs. (64)].

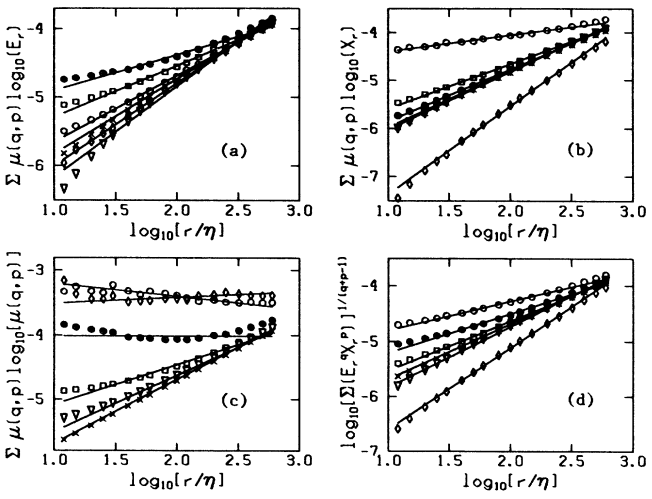

FIG. 3. Log-log plots obtained from the measurements in the heated wake of a cylinder, corresponding to different choices of q and p. Starting clockwise from the upper left, the slopes of the linear fits (using a scaling range of $r/\eta=30$ to 250; solid lines) correspond to $\alpha(q,p)$ $\alpha'(q,p)$, $\tau(q,p)/(q+p-1)$, and $f(\alpha,\alpha')$. Circles with + correspond to $(q,p)=(4,0)$; circles$=(0,4)$; squares $=(0.5,2)$; $\times=(0,0)$; triangles $=(-1,0)$ and diamonds $=(0,-4)$.

At any rate, it appears that the best linear fit can be obtained in a range between $r/\eta=30$ and $r/\eta=250$. The fits were then obtained automatically for all 17^2 pairs of (q,p). Such fits are shown as solid lines in Figs. 3. In order to obtain a qualitative idea about the uncertainty of the results because of the precise selection of the scaling range, the fits were also made in a range at smaller scales ($r/\eta=20$ to $r/\eta=100$), and in a range at larger scales ($r/\eta=40$ to $r/\eta=400$).

For the second method of using shorter data sets when computing the quantities in (73)–(77), we observe from the figures in the Appendix that the linear regimes are somewhat more extensive, but also that there is larger scatter in the data points. Shown as solid lines are linear least-square error fits through the points in a range between $r/\eta=25$ and $r/\eta=400$. The procedure is repeated for 20 data sets, and the exponents are obtained by fitting automatically for all 17^2 pairs of (q,p). The results vary somewhat from one data set to another, but the mean of all 20 realizations is used as representative. The corresponding standard deviations have also been computed.

The results of both procedures are given in the next section.

C. Results

By the procedures outlined in the previous section, we obtain $\alpha(q,p)$, $\alpha'(q,p)$, $f(q,p)$ and $\tau(q,p)$. Next we can obtain $f(\alpha,\alpha')$ as an explicit function of α and α' by interpolating the f values on an equally spaced mesh in α and α'. The resulting contour plot is shown in Fig. 4 for the long-term averaging method. Figures 5(a) and 5(b) show $f(\alpha,\alpha')$ resulting from the use of the other scaling ranges $r/\eta=40$ to 400 and $r/\eta=20$ to 100, respectively. This gives an estimate of the uncertainty of the results associated with the selection of the precise scaling range. Figure 6 shows the mean $f(\alpha,\alpha')$ obtained from all the realizations of the short-term method. Figure 7(a) shows this mean result minus two standard deviations of the individual results, and Fig. 7(b) shows the mean $f(\alpha,\alpha')$

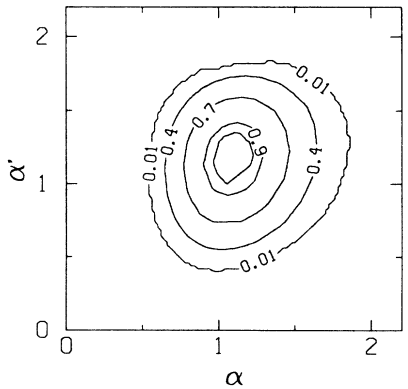

FIG. 4. Positive (manifest) portion of $f(\alpha,\alpha')$, obtained from log-log plots like Figs. 3 using long-term averaging. Lines are iso-f values corresponding to $f(\alpha,\alpha')=0.01$, 0.4, 0.7, 0.9, and 0.95. This contour plot represents the fractal dimensions of iso-(α,α') sets of the joint multifractal distribution of ε and χ in the turbulent wake of a heated cylinder. The scaling range used to obtain this result was from $r/\eta=30$ to 250.

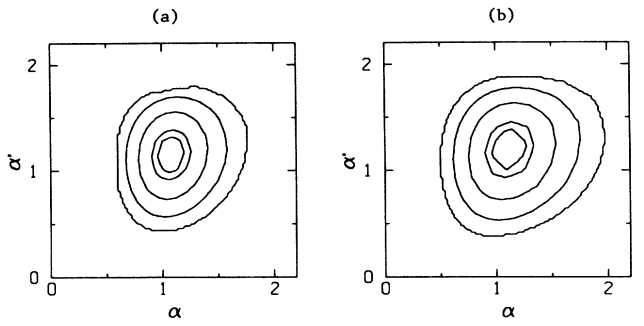

FIG. 5. Analysis of the sensitivity of $f(\alpha,\alpha')$ on the scaling range used. (a) shows the contour plots of $f(\alpha,\alpha')$ using a range of $r/\eta=40$ to 400. (b) shows the contour plots using a range of $r/\eta=20$ to 100. The contour lines represent the same levels as the ones in Fig. 4. The sensitivity is relatively high due to the moderate Reynolds number of the flow.

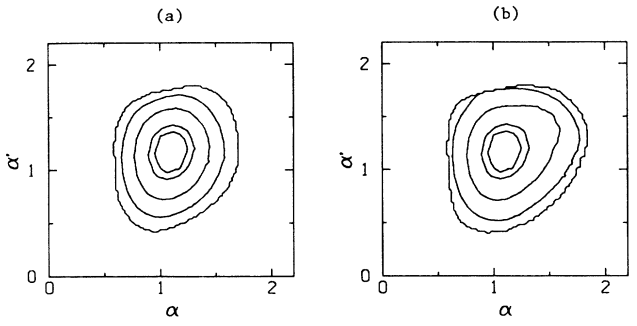

FIG. 7. Illustration of the variability of $f(\alpha,\alpha')$ from one realization to another, using short-term averages. In (a) we plot the mean of $f(\alpha,\alpha')$ minus twice its standard deviation, and in (b) we plot the mean of $f(\alpha,\alpha')$ plus twice its standard deviation. The contour lines represent the same levels as the ones in Fig. 6.

plus two standard deviations of the individual results. This gives an estimate of the uncertainty of the result associated with the individual shorter averages.

Figures 4 and 6 are the main results of this section. They are the positive (manifest) part of $f(\alpha,\alpha')$ for one-dimensional intersections through the joint field of ε' and χ'. Due to the relatively moderate Reynolds number of the flow, the uncertainty of the results is quite large as seen from the magnitude of the error estimates in Figs. 5 and 7. However, we believe that the main features of the joint multifractal distribution of ε' and χ' are clearly visible is these results. We also note that both results from long-term averaging and the mean of short-term averaging are similar, the differences being of the order of the uncertainty itself. The difference is larger at the low intensity part of the distribution, where the influence of noise, and the occasional "irrotational" portions of the signals (see Ref. 12) are of relevance.

Let us now briefly remark on the distribution of α and α' separately. We see from Fig. 4 and 6 that the limits of α (singularity strengths of ε') are $\alpha_{\min}\approx 0.5$ and $\alpha_{\max}\approx 1.8$ (where $f=0$ on the linear cut), in agreement with the results of Ref. 9. Also, the limits of α' (singularity strengths of χ') are $\alpha'_{\min}\approx 0.4$ and $\alpha'_{\max}\approx 1.8$, in rough agreement with the result of Refs. 13 and 14.

In order to allow for a more detailed comparison with previous measurements, we notice that $f(\alpha)$, the fractal dimension of an iso-α set, can be obtained as a function of $f(\alpha,\alpha')$ by noting that

$$\Pi_r(\alpha)d\alpha=\int_{\alpha'}\Pi_r(\alpha,\alpha')d\alpha\,d\alpha'\sim r^{\,d-\max_{\alpha'}f(\alpha,\alpha')}\,, \tag{78}$$

for small r. Therefore

$$f(\alpha)=\max_{\alpha'}f(\alpha,\alpha')\,. \tag{79}$$

Similarly $f'(\alpha')$, the dimension of iso-α' sets is given by

$$f'(\alpha')=\max_{\alpha}f(\alpha,\alpha')\,. \tag{80}$$

Figure 8 shows a comparison between $f(\alpha)$ obtained from $f(\alpha,\alpha')$ via Eq. (79) and that measured in Ref. 9.

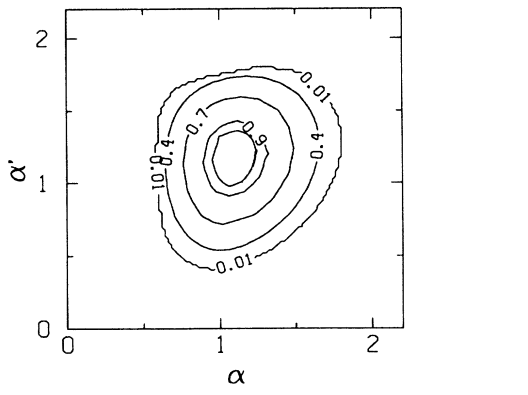

FIG. 6. Positive (manifest) portion of $f(\alpha,\alpha')$, corresponding to the mean of 20 short-term results (see Appendix). The scaling range used to obtain this result was from $r/\eta=25$ to 400.

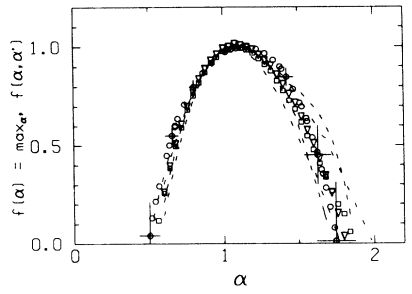

FIG. 8. Comparison of $f(\alpha,\alpha')$ with previous results on $f(\alpha)$ of the single multifractal distribution of ε'. Circles and error bars correspond to the mean and uncertainty of the results of Ref. 9. Squares are the maximum of $f(\alpha,\alpha')$ over α', using long-term averaging. This is the dimension of iso-α sets, for any α' value. Triangles correspond to the mean value of $\max_{\alpha'}f(\alpha,\alpha')$ using short-term averaging. The dashed lines represent the sensitivity on the scaling range for the long-term averaging, and again two standard deviations for the short-term averaging.

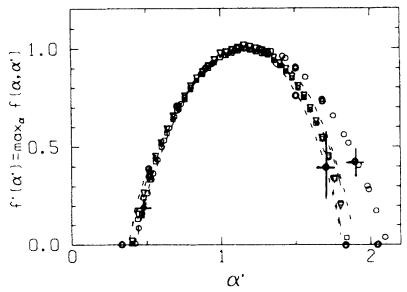

FIG. 9. Comparison of $f(\alpha,\alpha')$ with previous results on $f'(\alpha')$ of the single multifractal distribution of χ'. Circles and error bars correspond to the mean and uncertainty of the results of Refs. 12 and 14. Squares are the maximum of $f(\alpha,\alpha')$ over α using the long-term averaging. This is the dimension of iso-α' sets, for any α value. Triangles correspond to the mean value of $\max_\alpha f(\alpha,\alpha')$ using short-term averaging. The dashed lines represent the sensitivity on the scaling range for the long-term averaging, and again two standard deviations for the short-term averaging.

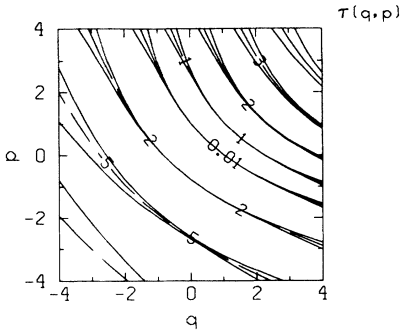

FIG. 11. Contour plots of $\tau(q,p)$ measured from slopes of plots like Figs. 28–30 (see Appendix) using short-term averages. The bundles of contour lines correspond to $\tau=-10$, -5, -2, 0.01, 1, 2, 3, and 4. The curves in the middle of each bundle correspond to the mean of the 20 realizations (see Appendix); the other two correspond to the mean value plus and minus two standard deviations.

They agree with each other within the experimental uncertainty. Figure 9 shows $f'(\alpha')$ obtained from Eq. (80) and from Refs. 13 and 14. Except for the right-most part of the curve (which is influenced by noise), the agreement is quite good.

Returning to the general shape of $f(\alpha,\alpha')$, we notice that it is stretched in the α' direction, consistent with the previous observation that χ' is more intermittent than ε'. However, it is not very eccentric and tilted, which seems to suggest that α and α' are not strongly correlated. This will be quantified using the moment exponents $\tau(q,p)$ below.

The function $\tau(q,p)$ is shown in the form of contour plots in Figs. 10 and 11, again for both averaging methods. The different bundles of lines in Fig. 10 correspond to different iso-$\tau(q,p)$ values. The middle line in each bundle is obtained from fits using the scaling range $r/\eta=30$ to 250 on the long-term results; the other two lines correspond to other scaling ranges mentioned above, and thus give an estimate of the sensitivity of $\tau(q,p)$ on the selection of the scaling range. The middle lines in Fig. 11 correspond to the mean value of $\tau(q,p)$ from the 20 realizations of the short-term method, and the other lines correspond to twice the standard deviation on either side of the mean. [To check the validity of Eqs. (32), we obtained $\alpha(q,p)$, $\alpha'(q,p)$, and $f(\alpha,\alpha')$ by evaluating the first derivatives of $\tau(q,p)$. The results are indistinguishable from those of Figs. 4 and 6.]

In order to compute the second-order derivatives of τ (or first derivatives of α and α') required to obtain μ,μ' and ρ, we plot in Figs. 12(a) $\partial^2\tau/\partial q^2$ for $p=0$ as a function of q, and in 12(b), $\partial^2\tau/\partial p^2$ for $q=0$ as a function of p. To compute ρ, we plot $\partial^2\tau/\partial q\,\partial p$ for $p=0$ as a function of q in Fig. 12(c) and for $q=0$ as a function of p in Fig. 12(d). The derivatives are evaluated to order $O(\Delta q^2)$ using finite differences on the mesh with

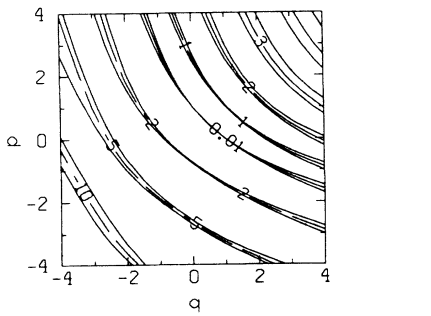

FIG. 10. Contour plots of $\tau(q,p)$ measured from slopes of plots like Figs. 3(d) using long-term averages. The bundles of contour lines correspond to $\tau=-10$, -5, -2, 0.01, 1, 2, 3, and 4. The curves in the middle of each bundle correspond to using a scaling range of $r/\eta=30$ to 250; the other two correspond to $r/\eta=40$ to 400 and $r/\eta=20$ to 100.

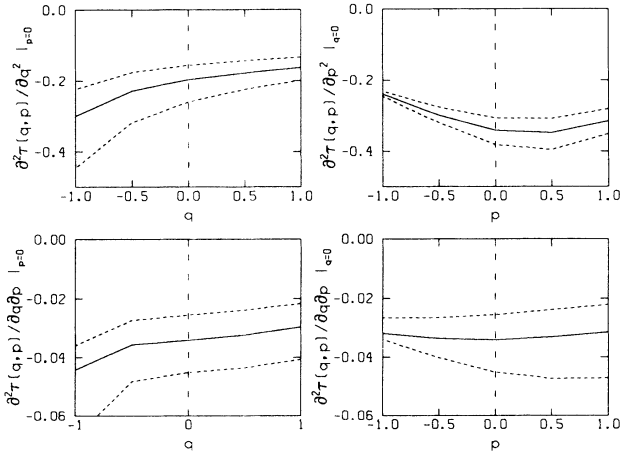

FIG. 12. Second-order derivatives of $\tau(q,p)$ along the q and p directions at $q=0$ and $p=0$, obtained from centered differences of the result of Fig. 10. The values of these curves at the origin correspond to (from the upper left corner clockwise) μ, μ', and ρ. The dashed lines correspond to the use of the scaling ranges $r/\eta=20$ to 100 and 40 to 400.

$\Delta q = 0.5$. The solid lines correspond to the derivatives of $\tau(q,p)$ obtained from fits in the central range of the long-term procedure. The dashed lines are obtained from the values of $\tau(q,p)$ corresponding to the other scaling ranges. The intercepts of these curves at $q=p=0$ are

$$\left.\frac{-\partial^2\tau}{\partial q^2}\right|_{0,0} = \mu \approx 0.20 \pm 0.05 \ , \tag{80a}$$

$$\left.\frac{-\partial^2\tau}{\partial p^2}\right|_{0,0} = \mu' \approx 0.34 \pm 0.05 \ , \tag{80b}$$

$$\left.\frac{-\partial^2\tau}{\partial p\,\partial q}\right|_{0,0} = \left.\frac{-\partial^2\tau}{\partial p\,\partial q}\right|_{0,0} \approx 0.034 \pm 0.01 \ . \tag{80c}$$

Figures 13(a)–13(d) show analogous results using $\tau(q,p)$ from the short-term averaging procedure. The results at $q=p=0$ are essentially similar to the long-term averaging ones, and we shall not use them here explicitly. Using the definition of ρ given in Sec. III D, we obtain $\rho \approx 0.13 \pm 0.04$. This relatively low degree of correlation is consistent with the general shape of $f(\alpha,\alpha')$. We have also computed the correlation coefficient of $\ln(\varepsilon_r)$ and $\ln(\chi_r)$ directly for different box sizes. The results (circles) are shown in Fig. 14. This is quite consistent with a value of 0.13 for ρ obtained through $\tau(q,p)$. The squares in Fig. 14 are the correlation coefficients of ε_r and χ_r.

A comparison is now appropriate between this value of ρ and the measurements of Refs. 29 and 30. There, the correlation coefficient of $\ln(\varepsilon_r)$ and $\ln(\chi_r)$ was measured in jets and the atmospheric surface layer for several values of r. Their results are considerably higher than the present ones, quite outside experimental uncertainty. This discrepancy may be due to the following reason: A problem that arises in jets is that the ratio of the fluctuating velocity to the sweeping velocity is not small, as opposed to wakes, where this ratio is indeed small. If one operates a hot wire at a high overheat (as was done in the

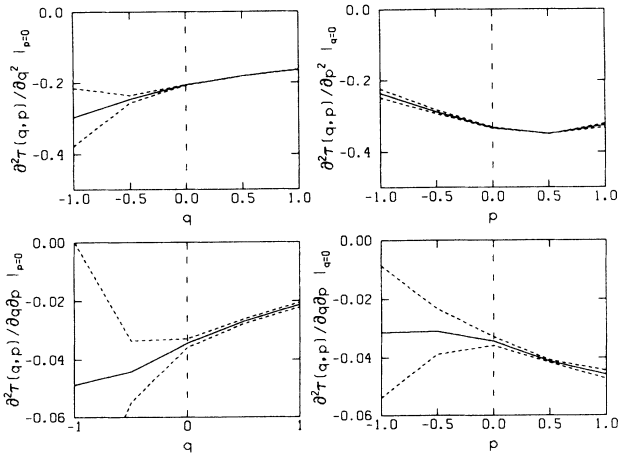

FIG. 13. Second-order derivatives of $\tau(q,p)$ along the q and p directions at $q=0$ and $p=0$, obtained from centered differences of the result of Fig. 11. The dashed lines correspond to the mean plus and minus two standard deviations, which is very small at the origin.

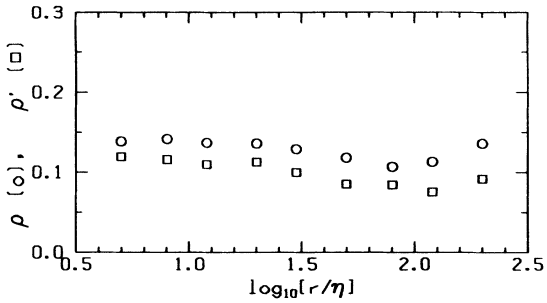

FIG. 14. Correlation coefficient of $\ln(\varepsilon_r)$ and $\ln(\chi_r)$ as a function of r (circles). Squares are the correlation coefficients of ε_r and χ_r.

above-mentioned references), there may be a strong influence of the hot wire on the cold-wire readings, thus artificially increasing the observed correlation between ε' and χ'. Our preliminary measurements in heated jets indeed confirm this possibility. This issue will be reported in detail in Ref. 33. This effect is not as severe in the atmospheric surface layer as in jets, and the somewhat smaller values of the correlation appear to be consistent with our conclusion that the correlation is indeed small if the two probes do not communicate with each other.

D. Implications on structure-function exponents of passive scalars

By dimensional analysis, it is usually[27] argued that the statistics of passive scalar differences $|\theta(x+r)-\theta(x)|$ should be similar to the statistics of $r^{1/6}\varepsilon_r^{-1/6}\chi_r^{1/2}$, where ε_r and χ_r are the rates of dissipation averaged in boxes of size r. Accordingly, one can write

$$\langle [\theta(x+r)-\theta(x)]^n \rangle = \langle \Delta\theta_r^n \rangle \sim r^{n/6} \langle \varepsilon_r^{-n/6} \chi_r^{n/2} \rangle \ . \tag{81}$$

Unlike the velocity-structure functions, $\langle \Delta\theta_r^n \rangle$ depends on both the joint statistics of χ and ε. Using $E_r = r\varepsilon_r$ and $X_r = r\chi_r$ on the linear sections through the dissipation fields, it follows that

$$\langle \Delta\theta_r^n \rangle \sim r^{\zeta_n} \ , \tag{82a}$$

where

$$\zeta_n = 1 + \tau(q = -n/6, p = n/2) \ . \tag{82b}$$

Thus we can obtain ζ_n from a cut through the $\tau(q,p)$ surface along the line $q=-p/3$. The values of $\tau(-n/6, n/2)$ were obtained from Figs. 10 and 11 for $n=0$ up to 8 by linear interpolation [since $\tau(q,p)$ is only available on a mesh of spacing $\Delta q = \Delta p = \frac{1}{2}$]. In Fig. 15, circles correspond to $1+\tau(q=-n/6, p=n/2)$ from measurements of the previous section using long-term averaging. Triangles correspond to results using short-term averaging. Dashed lines are the estimates of experimental uncertainty. Squares correspond to experimental

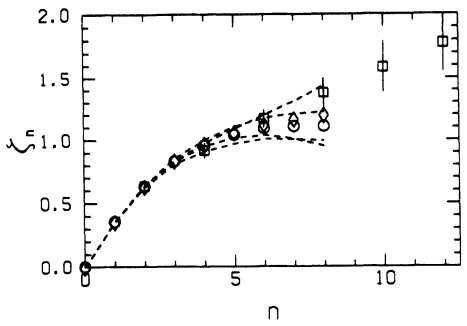

FIG. 15. Scaling exponents ζ_n of the temperature structure functions of order n. Squares are experimental results from Antonia *et al.* (Ref. 34). Circles are the results using the present results obtained from $\tau(q,p)$ using long-term averaging. Diamonds are from measurements using the mean of short-term averages. The dashed lines are again estimates of the uncertainty of the results.

results of ζ_n obtained by Antonia *et al.*[34] directly from temperature structure functions. The measurements agree quite well for n up to 6. For higher moments, our results fall below the results of Ref. 34. We will return to the data in the next section, but note here that the reason for the discrepancy for higher n is unknown. We also note that getting 12th-order structure functions reliably is quite demanding both in terms of length and stability of data.

E. Modeling of the joint distribution of ε' and χ'

Antonia *et al.*[34] compared their results on the scaling exponents of temperature structure functions to predictions by β models and joint log-normal distributions. Both types of models were shown to be inappropriate. As a digression, we write here the expression for ζ_n for the case of joint log-normal distributions for different intermittency exponents μ and μ'. The expression is

$$\zeta_n = n/3 - n(\mu - 3\mu')/12 - n^2[\mu - 6\rho(\mu\mu')^{1/2} + 9\mu']/72 , \tag{83}$$

which is obtained by substituting Eq. 52(d) into Eq. 82(b). For $\mu=\mu'$, this relation reduces to the equation given in Ref. 34.

Now we illustrate that a joint binomial model with the measured correlation can fit the joint multifractal spectrum quite well. We know from Ref. 11 that $f(\alpha)$ of ε' is well represented by a p model with $p_1=0.7$ and $p_2=0.3$. Similarly, $f'(\alpha')$ of χ' can be fitted reasonably well by a p model with $p_1'=3/4$ and $p_2'=\frac{1}{4}$. [These models are valid for the positive (manifest) portion of the $f(\alpha)$ curve of the one-dimensional cuts only.] We use our measured value of $\rho=0.13$ and use Eq. (63) to obtain $\tau(-n/6, n/2)$ for the joint binomial distribution.

The dot-dashed line of Fig. 16 shows the result for $\rho=0.13$. If we want to improve the fit, we see that $\rho=0.3$ seems more appropriate (solid line). Also, if we try to fit the results of Ref. 34 using joint binomial models with some higher value of ρ (e.g., $\rho=0.5$, the double dot-dashed line of Fig. 16), we see that it still asymptotes below the measurements of Ref. 34. The predictions of joint log-normal distributions for $\mu=0.20$, $\mu'=0.34$, and $\rho=0.13$ give the parabola shown in the bottom part of Fig. 16. The other parabola corresponds to $\rho=0.5$ but the same intermittency exponents. It is clear that they do not agree with the data, not even up to $n=6$.

Returning to joint binomial distributions, Fig. 17 shows the entire $f(\alpha,\alpha')$ for the case of $\rho=0.13$ and Fig. 18 for $\rho=0.3$. The overall agreement between the model and the observations in Figs. 4 and 6 is better for $\rho=0.13$. This leads one to ask why the agreement was better in regard to ζ_n for $\rho=0.3$ instead of 0.13. The reason is that $\langle \Delta T^n \rangle$ (for $n>0$) will be dominated by points where χ is high but ε is low, or where α' is low and α is high. This corresponds to the lower right quadrant of $f(\alpha,\alpha')$. In this region, we see that Fig. 18 is closer to the measurements. Thus, it appears that even though joint binomial models provide a useful "first-order" model for the joint distributions of ε' and χ', much superior to log-normal and β models, they do not reproduce every detail of the observations. For instance, the slight asymmetry of the lower-right and upper-left parts of Figs. 4

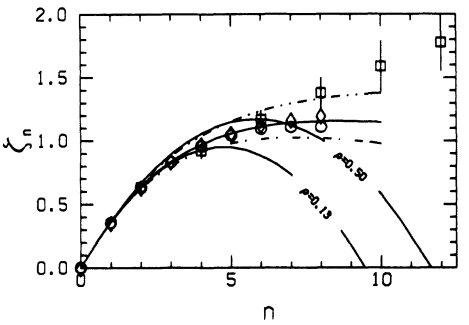

FIG. 16. Scaling exponents ζ_n of the temperature structure functions of order n. Symbols as in Fig. 15. The dot-dashed line is a joint binomial model with $p_1=0.7$, $p_1'=0.75$, and $\rho=0.13$. The solid line is the same model with $\rho=0.3$, which seems to fit the data better. The double dot-dashed line is for $\rho=0.5$. Joint log-normal distributions with $\mu=0.2$, $\mu'=0.34$, and $\rho=0.13$ or 0.5 give the two parabolas at the bottom.

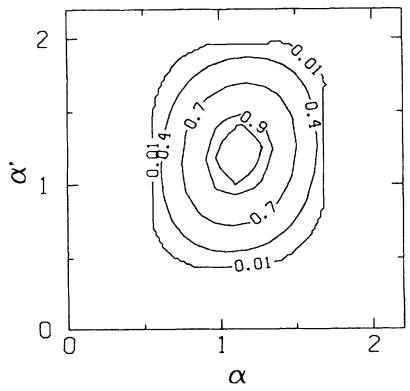

FIG. 17. Positive part of $f(\alpha,\alpha')$ of a joint binomial cascade with $p_1=0.7$, $p_1'=0.75$, and $\rho=0.13$. Lines are iso-f values corresponding to $f(\alpha,\alpha')=0.01$, 0.4, 0.7, 0.9, and 0.95.

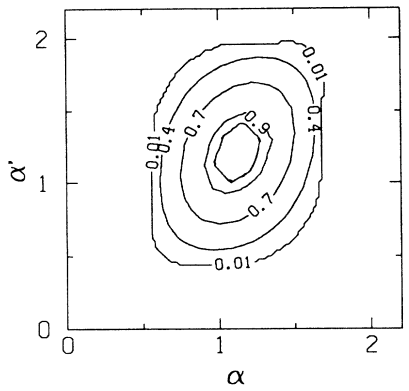

FIG. 18. Positive part of $f(\alpha,\alpha')$ of a joint binomial cascade with $p_1=0.7$, $p_1'=0.75$, and $\rho=0.50$. Lines are iso-f values corresponding to $f(\alpha,\alpha')=0.01$, 0.4, 0.7, 0.9 and 0.95.

and 6 suggests deviations from predictions of joint binomial models.

VI. JOINT MULTIFRACTAL DISTRIBUTION OF ε' AND ω_x^2

One of the dynamically most relevant quantities in a turbulent flow is the vorticity $\boldsymbol{\omega}=\nabla\times\mathbf{u}$. It is well-known that vorticity fluctuations are intermittently distributed. The square of the vorticity fluctuations is a positive definite quantity like energy or scalar dissipation, and can be addressed using the multifractal formalism. This has been done in Ref. 15, where the $f(\alpha)$ curve for a single component, namely the square of the "streamwise" component of the vorticity fluctuation, was presented from experimental data. The $f(\alpha)$ curve obtained using numerical data generated by directly solving the Navier-Stokes equations[35] are in essential agreement with the measured data.

The aim of the present section is to quantify the joint multifractal distribution of the square of the streamwise vorticity and the term ε' of the dissipation. Section VI A presents issues related to the experimental procedure, Sec. VI B contains a description of the data processing techniques, and the results are presented in Sec. VI C.

A. Experimental procedure

The streamwise vorticity probe with four sensor wires and eight prongs, according to the scheme described by Wallace,[36] was constructed and tested. Briefly, eight fine bead craft needles with diameters of 0.2 mm were used as the supporting prongs, and the MV20-Mullite ($3Al_2O_3\cdot 2SiO_2$) round four-bore rods were used as the probe body. The diameter of the Wallaston wire used as sensor wires is 5 μm and the distances between the planes containing opposite wires are 1.9 mm, so that their length-to-diameter ratio is about 380. This is sufficient to reduce conduction effects to the prongs. The wire angles varied between 44° and 46°.

The vorticity probe calibration was conducted in the 20×28-in.^{2} subsonic wind tunnel, and the flow for calibration was uniform and irrotational. By measuring the output voltage of each wire at various speeds over a certain range, the constants in King's law were determined for all four wires. More details about the probe geometry, technical design and construction as well as the calibration procedure can be found in Ref. 15.

Four sets of DANTEC 55M10 (constant-temperature anemometer) and DANTEC 55D26 (signal conditioner) were used for the four wires of the probe in the experiment. Those wires were operated at a resistance overheat ratio of 1.5. The characteristic frequency response of the vorticity probe was estimated to be 5000 Hz. Thus the setting of the low-pass filter of the signal conditioners at 4000 Hz was selected.

Data in the atmospheric boundary layer were taken on the roof of a four-story building on a sunny and windy day. The mean velocity of the wind was approximately 7 m/s. The position of the vorticity probe was horizontally set 2 m above that roof.

The acquired signals were digitized using a 12-bit-resolution high-speed analog-to-digital converter DT2821 with a multiplexer for multichannel analysis. The subsequent measurements were carried out in two steps. First, the instantaneous voltages from the four wires were digitized and stored on the hard disc of an IBM PC-AT computer; before digitizing, analog signals were monitored on an oscilloscope. Second, the instantaneous values from the output of the digitizer were computed to give the streamwise vorticity ω_x. All the data were later transfered to a VAX station II for further analysis related to multifractals.

Figures 19(a) and (b) show typical simultaneous traces of ε' and ω_x^2 along the same linear cut. Both have been normalized by their respective mean values. These segments of data reveal a stronger correlation than that between ε' and χ' in Fig. 1; this will be quantified in the subsequent sections.

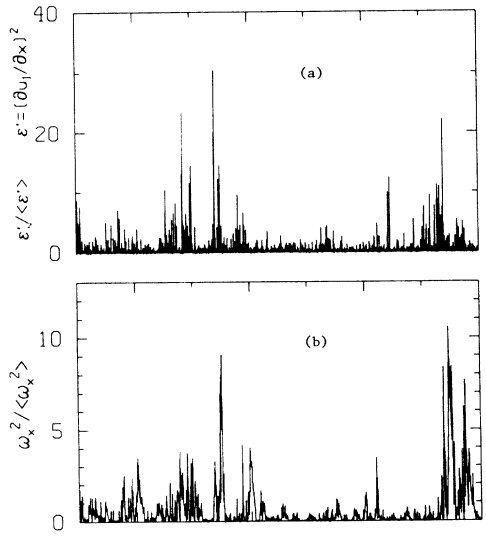

FIG. 19. Simultaneous signals of $\varepsilon'\sim(\partial u_1/\partial t)^2$ and ω_x^2 obtained in the atmospheric surface layer, both normalized by their own mean values.

B. Processing of data

In analogy with Eq. (68), we define $W_r(x)$ as the squared vorticity integrated over a box of size r according to

$$W_r(x_i)=\frac{\int_{x_i-r/2}^{x_i+r/2}\omega_x^2(x')dx'}{\int_0^L\omega_x^2(x')dx'} . \tag{84}$$

Again, if ε' and ω_x^2 form a joint multifractal distribution, we expect that

$$E_r(x_i)\sim r^{\alpha} \tag{85a}$$

$$W_r(x_i)\sim r^{\alpha'} , \tag{85b}$$

$$N_r(\alpha,\alpha')\sim r^{-f(\alpha,\alpha')} , \tag{85c}$$

in addition to

$$\sum_i[E_r(x_i)]^q[W_r(x_i)]^p\sim r^{\tau(q,p)} . \tag{85d}$$

We need to evaluate expressions like Eqs. (73)–(77) over all data points available from measurements. Here

$$\mu_r(x_i;q,p)=[E_r(x_i)]^q[W_r(x_i)]^p\Big/\sum_i[E_r(x_i)]^q[W_r(x_i)]^p . \tag{86}$$

For the atmospheric flow, the Reynolds number and the scaling range are expected to be considerably higher than for the laboratory flow of the previous section. However, since we have only about a tenth of the data, we expect the convergence of the higher moments to be incomplete. Figures 20(a)–20(d) show the value of the moments as a function of the length of the data set, and it can be seen that the values at $L=8\times10^5$ can still not be considered as converged. Nevertheless, the relative distance between the moments at different box sizes r does not fluctuate appreciably, meaning that the power-law exponent obtained from the appropriate log-log plots should not change too much as L is increased even further. We are thus inclined to believe that the data are adequately long to obtain good approximations of the scaling exponents.

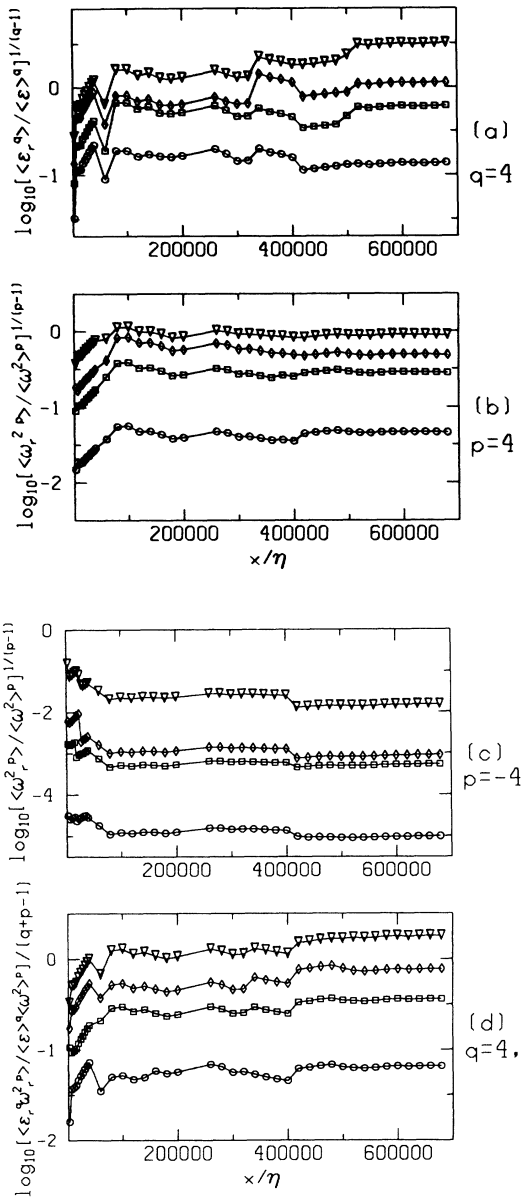

FIG. 20. Convergence of moments as a function of the length of the data. Different symbols correspond to different box sizes r. Circles, $r/\eta=10$; squares, $r/\eta=100$; diamonds, $r/\eta=300$; triangles, $r/\eta=1000$. (a) shows the convergence of the fourth moments of ε_r. (b) shows the same for ω_r^2, the local average of ω_x^2 over boxes of size r. In (c), we show the convergence of the fourth negative moment of ω_r^2, and (d) is for a mixed moment of order 8 ($q=4$, $p=4$).

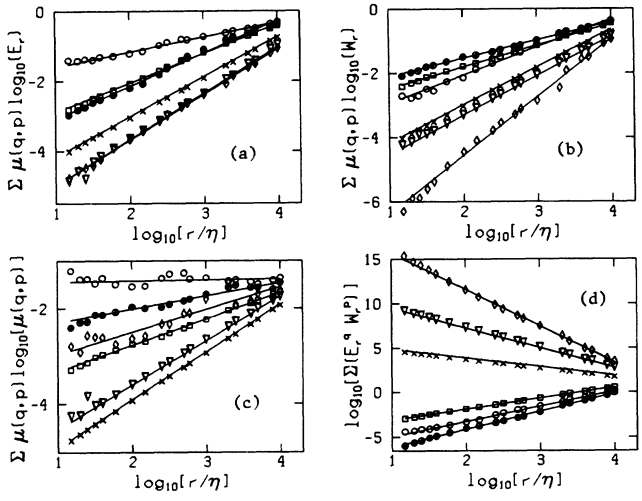

FIG. 21. Regression plots obtained from measurements in the atmospheric surface layer corresponding to different choices of q and p. Starting clockwise from the plot in the upper left corner, the slopes of the linear fits (using a scaling range of $r/\eta=35$ to 10^4; solid lines) correspond to $\alpha(q,p)$, $\alpha'(q,p)$, $\tau(q,p)$, and $f(\alpha,\alpha')$. Circles with + correspond to $(q,p)=(4,0)$; circles$=(0,4)$; squares$=(0.5,2)$; crosses$=(0,0)$; triangles $=(-1,0)$ and diamonds$=(0,-2)$.

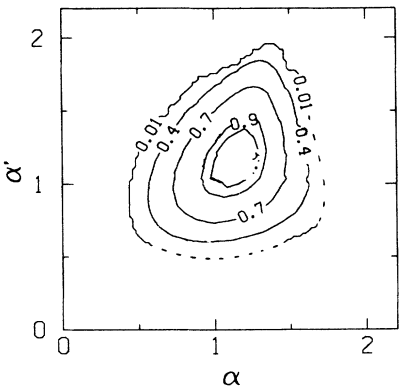

FIG. 22. Positive (manifest) portion of $f(\alpha,\alpha')$, obtained from log-log plots like Fig. 21. This contour plot represents the fractal dimensions of iso-(α,α') sets of the joint multifractal distribution of ε' and ω_x^2. The scaling range used to obtain this result was from $r/\eta=35$ to 10^4.

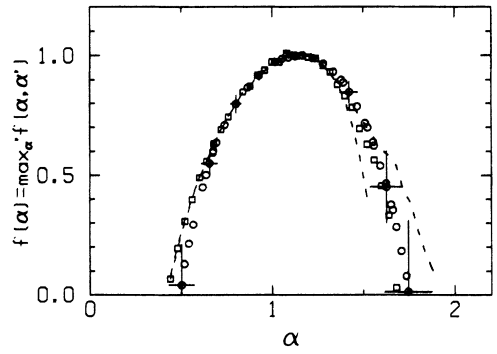

FIG. 24. Comparison of $f(\alpha,\alpha')$ with previous results on $f(\alpha)$ of the single multifractal distribution of ε'. Circles and error bars correspond to the mean and uncertainty of the results of Ref. 9. Squares are the maximum of $f(\alpha,\alpha')$ over α' which is the dimension of iso-α sets, for any α' value. The dashed lines represent the sensitivity on the scaling range.

As before, the computation of the sums is performed for a total of 17^2 pairs of (q,p) values ranging from -4 to $+4$, equally spaced at intervals of $\Delta q=0.5$. This is repeated for 24 values of different box-sizes from $r/\eta=10$ to 10^4. We then obtain the exponents α, α', f, and τ from the appropriate plots. Figures 21(a)–21(d) show a representative sample of such plots. The slopes of the solid lines (least-square error fits in a range $r/\eta=35$ to 10^4) correspond to $\alpha(q,p)$, $\alpha'(q,p)$, $f(q,p)$, and $\tau(q,p)$. The power-law behavior extends unambiguously over 2.5 decades.

C. Results

Next we obtain $f(\alpha,\alpha')$ as an explicit function of α and α' by again interpolating the f values on an equally spaced mesh in α and α'. The resulting contour plot is shown in Fig. 22. This figure is the main result of this section and represents the positive (manifest) part of $f(\alpha,\alpha')$ for one-dimensional intersections through the joint field of ε' and ω_x^2. Figures 23(a) and 23(b) show $f(\alpha,\alpha')$ resulting from the use of the other scaling ranges $r/\eta=25$ to 8×10^3 and $r/\eta=50$ to 10^4, respectively. The same iso-f contour lines as in Fig. 22 are shown. Together, these figures give an estimate of uncertainty associated with the choice of the precise scaling range. Due to the large scaling range, the uncertainty of the results is small in much of the contour plots. The error is large for the regions of high α, where ε' is low. The scatter of points in the regression plots is high for large negative values of q, probably due to noise and insufficient sampling length. However, the main features of the joint multifractal distribution of ε' and ω_x^2 are clearly visible in the results of Fig. 22.

Next we can apply again Eqs. (79) and (80) to obtain the single $f(\alpha)$ curves. The single $f(\alpha)$ of ε' is given in Fig. 24, where it is again compared to the previous results of Ref. 9. Both measurements agree within experimental scatter. Figure 25 is the $f'(\alpha')$ of ω_x^2, which is quite asymmetric with $\alpha_{\min}\approx0.5$ and $\alpha_{\max}\approx2$.

Figure 26 shows $\tau(q,p)$ for the joint distribution of ε' and ω_x^2. As in Sec. V, the uncertainty associated with the scaling range is represented by bundles of iso-τ lines. It is seen that the uncertainty is large when $q<0$.

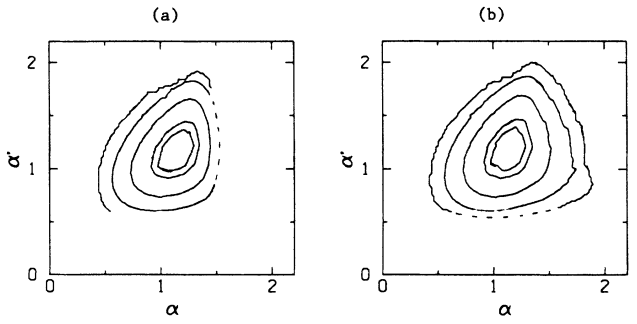

FIG. 23. Analysis of the sensitivity of $f(\alpha,\alpha')$ on the scaling range used. (a) shows the contour plots of $f(\alpha,\alpha')$ (same levels as in Fig. 22) using a range from $r/\eta=40$ to 10^4. (b) shows the contour plots using a range of $r/\eta=25$ to 8 000. The sensitivity is large only for $q<0$.

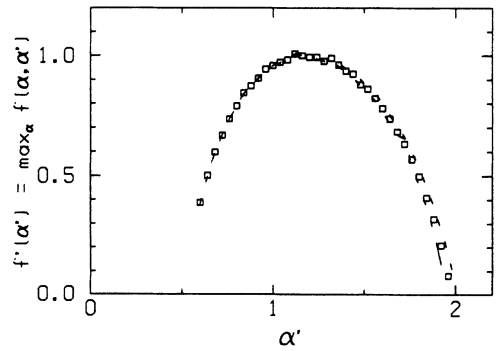

FIG. 25. $f'(\alpha')$ curve of the single distribution of ω_x^2 obtained from $f(\alpha,\alpha')$. The dashed lines represent the sensitivity on the scaling range.

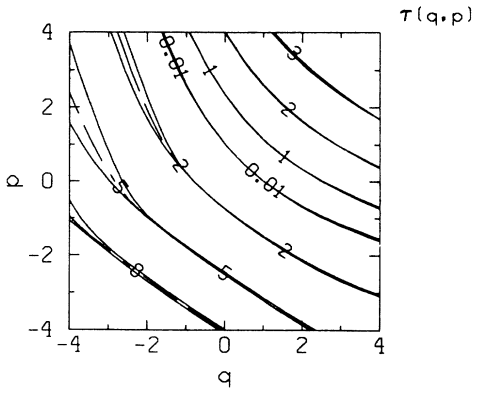

FIG. 26. Contour plots of $\tau(q,p)$ measured from slopes of plots like Figs. 21. The bundles of contour lines correspond to $\tau=-10, -5, -2, 0.01, 1, 2, 3$, and 4. The curves in the middle of each bundle correspond to using a scaling range $r/\eta=35$ to 10^4; the other two correspond to $r/\eta=25$ to 8000 and $r/\eta=50$ to 10000.

In order to quantify the intermittency and correlation exponents, we evaluate again the second-order derivatives of $\tau(q,p)$ using centered differences. The results are shown in Fig. 27. From the values at $q=p=0$, we infer

$$\mu=0.23\pm0.01 ,$$

$$\mu'=0.40\pm0.02 ,$$

and

$$\rho=0.3\pm0.03 .$$

The degree of correlation between ε' and ω_x^2 is thus considerably higher than between ε' and χ'.

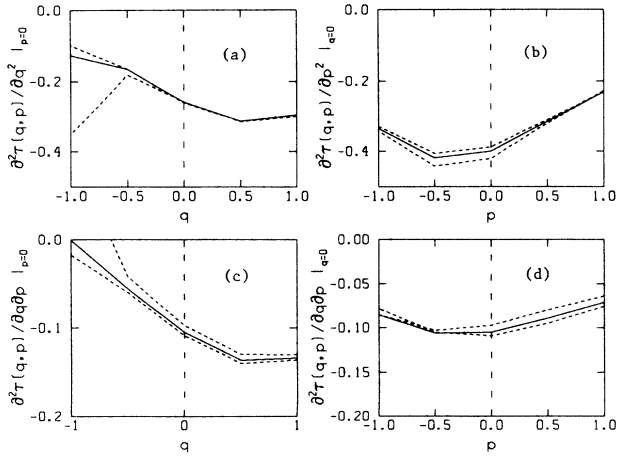

FIG. 27. Second-order derivatives of $\tau(q,p)$ along the q and p directions at $q=0$ and $p=0$, obtained from centered differences of the result of Fig. 26. The values of these curves at the origin correspond to (from the upper left corner clockwise) μ, μ', and ρ. The dashed lines correspond to the use of the scaling ranges $r/\eta=25$ to 8000 and 50 to 10^4.

VII. CONCLUSIONS

The multifractal formalism has been extended to multivariate measures. It was shown that such an extension is natural and useful for describing joint intermittent distributions, such as joint log-normal and joint binomial ones. It was also shown that second-order statistics of the local scaling exponents $\alpha^{(i)}$ could be described by a conveniently defined covariance matrix μ_{ij}. For the special case of bivariate distribution, we have defined intermittency exponents μ, μ', and a correlation exponent ρ. This formalism is then used to analyze measurements in fully developed turbulent flows.

In relation to the joint distribution of the "streamwise terms" ε' and χ' of the dissipations of kinetic energy and passive scalar fluctuations, we can conclude that they form a joint multifractal distribution. Their degree of correlation is relatively low, and can be quantified by $\rho=0.13$ (it must be stressed that such a result need not necessarily be the same as for the lateral and cross terms of the dissipation). The joint distribution of ε' and χ' can be related to the scaling exponents of temperature structure functions, and the results agree well with results of Ref. 34 for moments up to order 5. It was also shown that joint binomial distributions can model the observations much better than joint log-normal or β models. However, some important differences between such a modeling and the measurements are still visible and may point to dynamically important features.

A similar multifractal analysis of ε' and ω_x^2 has been presented from atmospheric data at high Reynolds number. The degree of correlation between these quantities is substantially higher ($\rho=0.3$) than that between ε' and χ'.

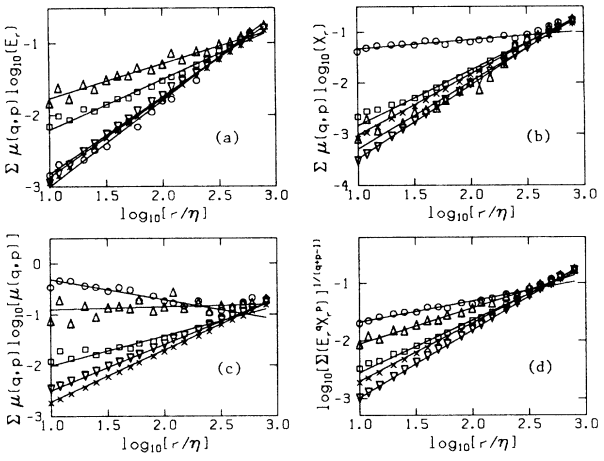

FIG. 28. Log-log plots obtained from the measurements from one realization plots of the short-term averaging procedure (see Sec. IV). Starting clockwise from the plot in the upper-left corner, the slopes of the linear fits (using a scaling range of $r/\eta=20$ to 400; solid lines) correspond to $\alpha(q,p)$, $\alpha'(q,p)$, $\tau(q,p)/[q+p-1]$, and $f(\alpha,\alpha')$. Different symbols correspond to different choices of q and p. Triangles correspond to $(q,p)=(4,0)$; circles$=(0,4)$; squares$=(0.5,2)$; crosses$=(0,0)$ and inverted triangles $=(0,-1)$.

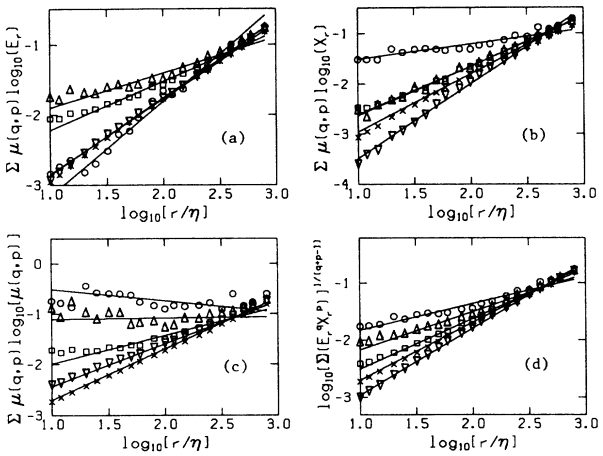

FIG. 29. As in Fig. 28, but for another realization.

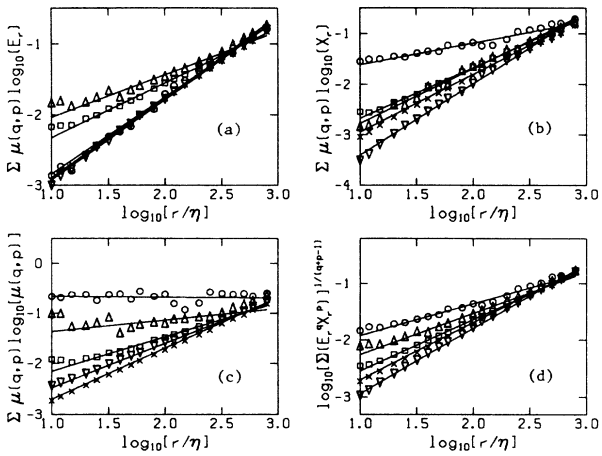

FIG. 30. As in Fig. 28, but for another realization.

ACKNOWLEDGMENTS

We are grateful to A. Chhabra, C. Evertsz, and Professor B. B. Mandelbrot for useful discussions, to Professor R. A. Antonia and Professor C. W. Van Atta for a brief conversation on the correlation between ε' and χ', and to the Defense Advanced Research Projects Agency (University Research Initiative), the Air Force Office of Scientific Research, and the National Science Foundation.

APPENDIX

In this appendix, we present some typical results from the method of using relatively short data sets to compute the scaling exponents. The experimental details and the data processing techniques were described in Sec. IV. Here we limit ourselves to a presentation of a representative sample of plots from which the exponents of Sec. IV are obtained. The results for five different choices of q and p are shown, namely (q,p)=(4,0), (0,4), (0.5,2), (0,0), and (0,−1). This is repeated for three segments of data, from Figs. 28–30. The solid lines are the linear least-square error fits using the points in a range $r/\eta=25$ to 400. The resulting slopes vary somewhat from one data segment to another, but these fluctuations occur around a representative mean value.

*Present address: Center for Turbulence Research, Stanford University, Stanford, CA 94305-3030.

[1]B. B. Mandelbrot, J. Fluid Mech. **62**, 331 (1975).

[2]U. Frisch and G. Parisi, in *Turbulence and Predictability in Geophysical Fluid Dynamics and Climate Dynamics*, edited by M. Ghil, R. Benzi, and G. Parisi (North-Holland, New York, 1985), p. 84.

[3]R. Benzi, G. Paladin, G. Parisi, and A. Vulpiani, J. Phys. A **17**, 3521 (1984).

[4]T. C. Halsey, M. H. Jensen, L. P. Kadanoff, I. Procaccia, and B. I. Shraiman, Phys. Rev. A **33**, 1141 (1986).

[5]M. H. Jensen, L. P. Kadanoff, A. Libchaber, I. Procaccia, and J. Stavans, Phys. Rev. Lett. **55**, 2798 (1985).

[6]D. J. Olinger and K. R. Sreenivasan, Phys. Rev. Lett. **60**, 797 (1988).

[7]T. C. Halsey, P. Meakin, and I. Procaccia, Phys. Rev. Lett. **56**, 854 (1986).

[8]G. Paladin and A. Vulpiani, Phys. Rep. **156**, 147 (1987).

[9]C. Meneveau and K. R. Sreenivasan, Nucl. Phys. B Proc. Suppl. **2**, 49 (1987).

[10]K. R. Sreenivasan and C. Meneveau, Phys Rev. A **38**, 6287 (1988).

[11]C. Meneveau and K. R. Sreenivasan, Phys. Rev. Lett. **59**, 1424 (1987).

[12]C. Meneveau, Ph.D. thesis, Yale University, 1989.

[13]R. R. Prasad, C. Meneveau, and K. R. Sreenivasan, Phys. Rev. Lett. **61**, 74 (1988).

[14]R. R. Prasad, C. Meneveau, and K. R. Sreenivasan (unpublished).

[15]S. Fan, Report No. FM01-88, Yale University, 1989 (unpublished).

[16]M. Blunt, Phys. Rev. A **39**, 2780 (1989).

[17]B. B. Mandelbrot, in *Fluctuations and Pattern Formation*, edited by H. E. Stanley and N. Ostrowski (Dordtrecht Kluwer, 1989).

[18]C. Meneveau and K. R. Sreenivasan, Phys. Lett. A **137**, 103 (1989).

[19]H. G. E. Hentschel and I. Procaccia, Physica D (Amsterdam) **8**, 435 (1983).

[20]A. Chhabra and R. V. Jensen, Phys. Rev. Lett. **62**, 1327 (1989).

[21]A. Chhabra, C. Meneveau, R. V. Jensen, and K. R. Sreenivasan, Phys. Rev. A **40**, 5284 (1989).

[22]In terms of D_q, one obtains $\mu=-(d^2D_q/dq^2+2dD_q/dq)_{q=0}$. We had previously (Ref. 9) defined an intermittency exponent in terms of the slope of D_q at $q=0$ according to

$\mu_{\text{old}} = -2(dD_q/dq)_{q=0}$. Near $q=0$, d^2D_q/dq^2 is usually quite small, so that both definitions are numerically close in most cases, but the present definition is more consistent with the statistics of α.

[23]The present discussion focuses exclusively on the joint but single-point statistics. In a forthcoming publication, it will be shown that a self-consistent description of multiple-point statistics of multifractals can be achieved in terms of $f(\alpha)$. A combination of these ideas with the present ones should yield expressions for joint multiple-point statistics, etc.

[24]B. B. Mandelbrot, in *Statistical Models and Turbulence,* edited by M. Rosenblatt and C. W. Van Atta (Springer, New York, 1972), p. 333.

[25]C. W. Van Atta, Phys. Fluid **14**, 1803 (1971).

[26]L. F. Richardson, *Weather Prediction by Numerical Procedure* (Cambridge University Press, Cambridge, England, 1922); A. N. Kolmogorov, C. R. Acad. Sci. URSS, **30**, 299 (1941); A. M. Obukhov, *ibid.* **32**, 22 (1941); L. Onsager, Phys. Rev. **68**, 286 (1945); C. F. von Weizsäcker, Z. Phys. **124**, 614 (1948); W. Heisenberg *ibid.* **124**, 628 (1948); A. N. Kolmogorov, J. Fluid Mech. **13**, 82 (1962); A. M. Obukhov, *ibid.* **13**, 77 (1962); E. A. Novikov and R. W. Stewart, Isv. Akad. Nauk SSSR, Ser. Geofiz. **3**, 408 (1964); E. A. Novikov, Prikl. Mat. Mekh. **35**, 266 (1971) [Appl. Math. Mech. **35**, 231 (1971)]; U. Frisch, P. L. Sulem and M. Nelkin, J. Fluid Mech. **87**, 719 (1978).

[27]A. S. Monin and A. M. Yaglom, *Statistical Fluid Mechanics* (MIT Press, Cambridge, MA, 1971).

[28]H. Tennekes and J. L. Lumley, *A First Course in Turbulence* (MIT Press, Cambridge, MA, 1972).

[29]R. A. Antonia and C. W. Van Atta, J. Fluid Mech. **67**, 273 (1975).

[30]R. A. Antonia and A. J. Chambers, Boundary-Layer Meteorol. **18**, 399 (1980).

[31]R. Peattie, J. Phys. E **20**, 565 (1987).

[32]K. R. Sreenivasan, R. R. Prasad, C. Meneveau, and R. Ramshankar, Pure Appl. Geophys. J **131**, 297 (1989).

[33]P. Kailasnath *et al.* (unpublished).

[34]R. A. Antonia, E. J. Hopfinger, Y. Gagne, and F. Anselmet, Phys. Rev. A **30**, 2704 (1984).

[35]A. Dean and L. Keefe (unpublished).

[36]J. M. Wallace, Exp. Fluids **4**, 61 (1986).